

Rapid and sustained environmental responses to global warming: The Paleocene–Eocene Thermal Maximum in the eastern North Sea

Ella W. Stokke¹, Morgan T. Jones¹, Lars Riber², Haflidi Haflidason^{3,4}, Ivar Midtkandal², Bo Pagh Schultz⁵, and Henrik H. Svensen¹

¹CEED, University of Oslo, PO Box 1028, 0315 Oslo, Norway

²Department of Geosciences, University of Oslo, P.O. Box 1047, Blindern, NO 0316 Oslo, Norway

³Department of Earth Science, University of Bergen, Allégt. 41, N-5007 Bergen, Norway

⁴Bjerknes Centre for Climate Research, Jahnebakken 5, 5007 Bergen, Norway

⁵Museum Salling, Fur Museum, Nederby 28, 7884 Fur, Denmark

Correspondence to: Ella W. Stokke (e.w.stokke@geo.uio.no)

Abstract

The Paleocene–Eocene Thermal Maximum (PETM; ~55.9 Ma) was a period of rapid and sustained global warming associated with significant carbon emissions. It coincided with the North Atlantic opening and emplacement of the North Atlantic Igneous Province (NAIP), suggesting a possible causal relationship. Only a very limited number of PETM studies exist from the North Sea, despite its ideal position for tracking the impact of both changing climate and the NAIP ~~explosive and effusive~~ activity. Here we present sedimentological, mineralogical, and geochemical proxy data from Denmark in the eastern North Sea, exploring the environmental response to the PETM. An increase in the chemical index of alteration and a kaolinite content up to 50 % of the clay fraction indicate an influx of terrestrial input shortly after the PETM onset and during the recovery, likely due to an intensified hydrological cycle. The volcanically derived minerals zeolite and smectite comprise up to 36 % and 90 % of the bulk and clay mineralogy respectively, highlighting the NAIPs importance as a sediment source for the North Sea and in increasing the rate of silicate weathering during the PETM. XRF element core scans also reveal possible hitherto unknown NAIP ash deposition both prior to and during the PETM. Geochemical proxies show that an anoxic to sulfidic environment persisted during the PETM body, ~~possibly reaching euxinic conditions particularly~~ in the upper half of the PETM body stratigraphy with high concentrations of Mo (~~MO_{EF}>30>30 ppm~~), U (U_{EF} up to 5), S (~4 wt%), and pyrite (~7 % of bulk), ~~and low Th/U (<2 ppm)~~. At the same time, export productivity and organic matter burial reached its maximum intensity. These new records reveal that negative feedback mechanisms including silicate weathering and organic carbon ~~sequestration drawdown~~ rapidly began to counteract the carbon cycle perturbations and temperature increase, and remained active throughout the PETM. This study highlights the importance of shelf sections in tracking the environmental response to the PETM climatic changes, and as carbon sinks driving the PETM recovery.

1. Introduction

The early Cenozoic was a period characterized by long-term warming, punctuated by transient periods of rapid global hyperthermal events (Zachos et al., 2008; Hollis et al., 2012; Cramwinckel et al., 2018). The most pronounced of these periods was the Paleocene–Eocene Thermal Maximum (PETM; ~55.9 Ma; Kennett and Stott, 1991; Thomas and Shackleton, 1996; Westerhold et al., 2018), during which global surface temperatures rose rapidly by 4–5 °C (Dunkley Jones et al., 2013; Frieling et al., 2017). The PETM is associated with a large input of ^{12}C -rich carbon to the ocean–atmosphere system resulting in a 2.5–7.8 ‰ negative carbon isotope excursion (CIE) in the terrestrial and marine sedimentary record (McInerney and Wing, 2011). The PETM CIE lasted up to 200 kyr (Westerhold et al., 2018), and is characterised by a rapid onset (~1–5 kyr; Kirtland-Turner et al., 2017), followed by a stable body (~100 kyr; van der Meulen et al., 2020) and a gradual recovery towards background conditions (McInerney and Wing, 2011). There were a number of smaller-magnitude hyperthermals in the early Eocene, but the PETM differs from these events with both ~~greater~~ higher magnitude and longer duration (Zachos et al., 2010; Bowen, 2013). However, there is still no consensus on the ultimate PETM cause, or whether several mechanisms contributed to prolong the PETM duration (e.g. Zeebe et al., 2009; Bowen et al., 2015). Several ^{12}C -enriched carbon sources may have contributed to the PETM CIE: the dissociation of methane clathrates (Dickens et al., 1995), a bolide impact activating terrestrial carbon reservoirs (Kent et al., 2003; Schaller et al., 2016), and volcanic and thermogenic degassing from the North Atlantic Igneous Province (NAIP; Fig. 1; Eldholm and Thomas, 1993; Svensen et al., 2004; Storey et al., 2007a).

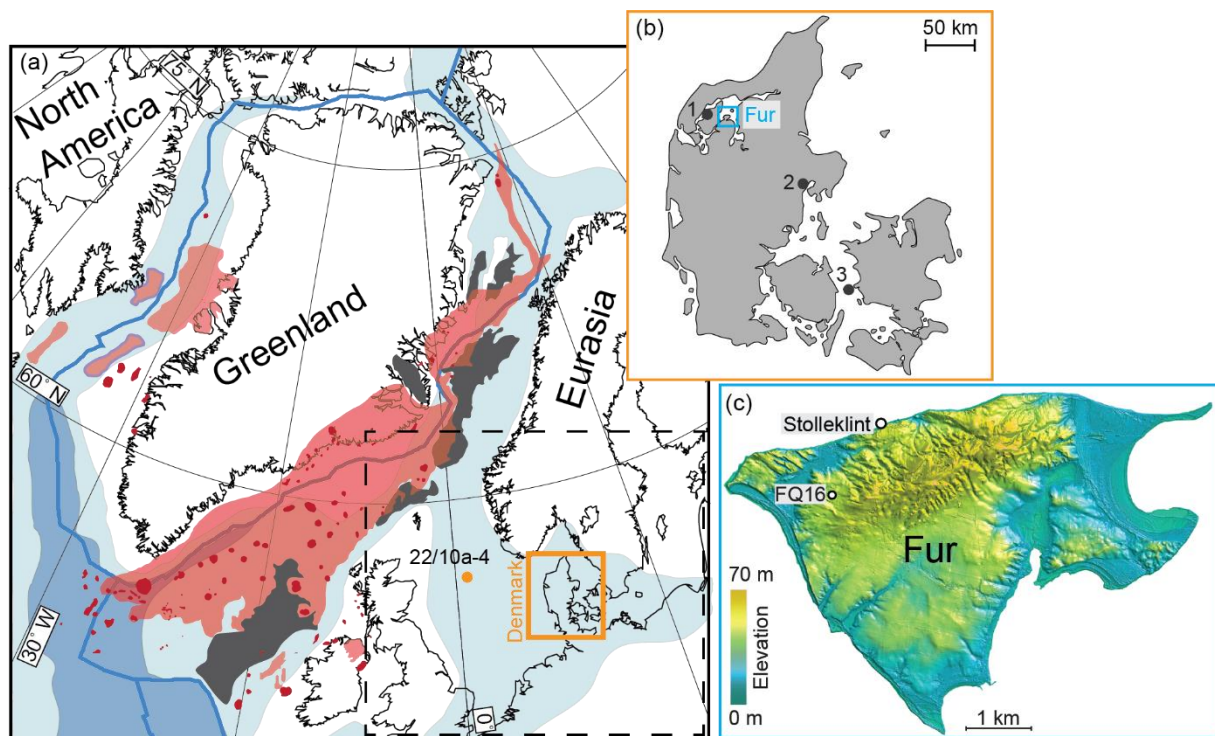


Figure 1: ~~a) Plate tectonic reconstruction~~ Palaeogeographic map from 56 Ma with the known NAIP extent indicated (modified from Abdelmalak et al., 2016, Horni et al., 2017, and Jones et al., 2019). The orange dot notes the position of core 22/10a-4 described by Kender et al. (2012) and Kemp et al. (2016). Blue lines: plate boundaries. Black lines: present-day coastlines. Light and dark blue areas: shelf and deep marine areas, respectively. Light red areas: Known extent of subaerial and submarine extrusive volcanism from the NAIP. Dark red: individual volcanic centres. Black areas: extent of known NAIP sill intrusions

in sedimentary basins. The total extent of intrusions beneath the extrusive volcanism is not known. The dashed square indicates the position of Figure 12. **(a)** Map of Denmark ~~showing with the~~ locations of the study area Fur. Additional locations from other relevant studies are indicated as: 1=Mors, 2=Ølst and 3=Store Bælt, indicated (b) Topographic map of the island of Fur (22 km²) with the two sample sites indicated. The high topography in the north of the island is a partially overturned anticline of Fur Formation and upper Stolleklint Clay strata. ~~FigureMap~~ modified from Stokke et al. (2020a).

Marine uptake of increased atmospheric CO₂ altered the ocean chemistry, leading to deep ocean acidification and substantial deep-sea carbonate dissolution (Zachos et al., 2005; Babila et al., 2018). The temperature increase and ocean acidification were accompanied by transient ocean circulation changes, increased halocline stratification and a global reduction in bottom water oxygen (Kennet and Stott, 1991; Nunes and Norris, 2006; Kender et al., 2012; Pälke et al., 2014). This led to the extinction of 30–50 % of all benthic foraminifera species (~~Koeh et al., 1992~~ Thomas, 1990; Thomas & Shackleton, 1996; Alegret et al., 2009; Nagy et al., 2013). Anoxic conditions were less extensive during the PETM than in previous ocean anoxic events (Jenkyns, 2010), and there were large regional variations in ocean oxygentionicity (Pälke et al., 2014). Still, globally widespread ocean deoxygenation has been recognised (Pälke et al., 2014; Zhou et al., 2014; Yao et al., 2018), with particularly prevalent anoxic to euxinic conditions observed in semi-enclosed shelf areas such as in the Tethys Ocean (Egger et al., 2003; Khozyem et al., 2013), Peri Tethys Basin (Gavrilov et al., ~~1997~~2003; Speijler et al., 1997; Dickson et al., 2014), the North Sea (Schoon et al., 2015), and the Arctic Ocean (Stein et al., 2006; Harding et al., 2011).

The hydrological cycle also changed substantially during the PETM (e.g. Carmichael et al., 2017), with modelling studies suggesting an overall increase in extreme weather events (Carmichael et al., 2018). Proxy evidence indicates a more humid climate, particularly in higher latitudes and marginal marine areas such as Antarctica (Robert and Kennett, 1994), the northeast US coast (Gibson et al., 2000; John et al., 2012), the Tethys (Bolle et al., 2000; Egger et al., 2003; Khozyem et al., 2013), North Atlantic (Bornemann et al., 2014), North Sea (Kender et al., 2012; Kemp et al., 2016), and the Arctic (Dypvik et al., 2011; Harding et al., 2011). In contrast, areas such as the Pyrenees (Schmitz and Pujalte, 2003) and the US interior (Kraus and Riggins, 2007) show evidence of arid climates. There seems to be considerable regional and temporal variation in the hydrological changes, with an increased meridional transport of water vapour from low to high latitudes leading to an overall dry–dryer, wet–wetter climate response to the global warming (Carmichael et al., 2017).

The 4–5 °C PETM temperature increase (Dunkley Jones et al., 2013; Frieling et al., 2017) is comparable to that predicted in response to the current anthropogenic carbon emissions (e.g. Riahi et al., 2017). The PETM is therefore an important natural analogue for future greenhouse conditions, as the environmental and ecological response may hold clues for the consequences of present day global warming (Zachos et al., 2010; Alley, 2016; Penman and Zachos, 2018; Svensen et al., 2019). Model predictions suggest that the current global warming will lead to an enhanced hydrological cycle, akin to that indicated by PETM proxy records (Held and Soden, 2006; Seager et al., 2010; Trenberth, 2011). The intensification of both droughts and extreme weather events are already occurring in parts of the world, with substantial consequences for human settlements (e.g. Riahi et al., 2017). Similarly, a decrease in ocean oxygenation has been observed for the last 50 years, most likely resulting from the current global warming (Bograd et al., 2008; Stramma et al., 2012). The spread of marine anoxia is a well-known consequence of global warming, negatively affecting marine ecosystems as a whole (Stramma et al., 2008; Gilly et al., 2013). Understanding the timing and regional distribution of the environmental response to global warming in the past is therefore vital to meet the challenges of the future.

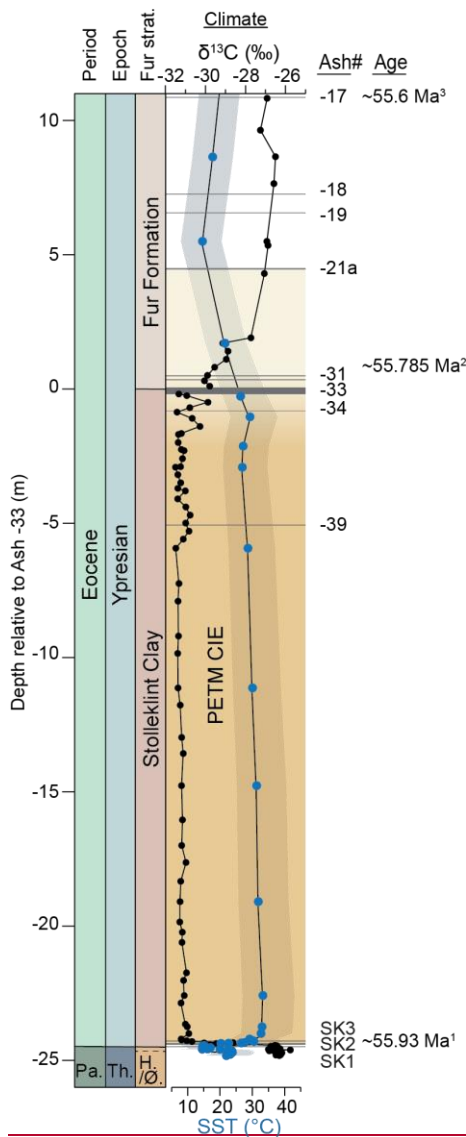


Figure 2: ~~H.Ø. Holmehus/Østerende Formation.~~ Data from the Stolleklint beach and a nearby quarry (Fig. 3), with lithological units indicated to the left. ~~H.Ø. Holmehus/Østerende Formation.~~ The depth scale is measured upwards and downwards from the main marker bed Ash -33. The yellow column indicates the interpreted PETM CIE duration, based on the $\delta^{13}\text{C}$ curve from Jones et al. (2019). The base of the column marks the CIE onset, and the gradually lighter colours toward the top marks the CIE recovery. Sea surface temperature (SST) variations are given as BAYSPAR-calibrated TEX_{86} SSTs with 1 σ error bar indicated by the light blue area (Stokke et al., 2020a). Ages are indicated based on ¹Westerhold et al., 2018; ²Charles et al. (2014), assuming the Svalbard and Fur CIEs timing is coeval; ³Age of Ash -17 from Storey et al. (2007a) recalibrated by Jones et al. (2019).

The Stolleklint section on the island of Fur in northwest Denmark offers an excellent opportunity to study the environmental response to temperature changes during the PETM in detail (Fig. 1). Denmark is placed in the eastern part of the epicontinental North Sea, which during the latest Paleocene became a highly restricted basin due to NAIP thermal uplift (Knox et al., 2010). During the PETM the North Sea was characterised by bottom-water deoxygenation (Schoon et al., 2015), and a high sedimentary input, significant surface water freshening, and development of halocline stratification reflecting an intensified hydrological cycle (Zacke et al., 2009; Kender et al., 2012; Kemp et al., 2016). At Stolleklint, the PETM is recognized by a 4.5 ‰ CIE and the appearance of the

diagnostic dinoflagellate *Apectodinium augustum* at the base of the earliest Eocene Stolleklint Clay (Fig. 2; Heilmann-Clausen, 1994; Schmitz et al., 2004; Schoon et al., 2013; Jones et al., 2019). The Stolleklint Clay – which covers the PETM interval in Denmark – is a thermally immature and expanded clay-dominated section unit, making this a unique and particularly well-suited section for detailed geochemical analyses. Located in a downwind direction and within proximity to the NAIP, Denmark was also ideally placed to record the contemporary volcanic activity from the NAIP (Fig. 1) that lasted between ~63-54 Ma (Fig. 1; Jones et al., 2019; Stokke et al., 2020b; Wilkinson et al., 2017). This is evidenced by the hundreds of NAIP tephra layers interbedded in the Danish and North Sea stratigraphy, mainly deposited during the most voluminous phase of the NAIP between ~56-54 Ma (Fig. 2; Bøggild, 1918; Knox and Morton, 1988; Larsen et al., 2003). The NAIP importance in the PETM initiation and termination is a topic of much discussion (Svensen et al., 2004; Jolley and Widdowson, 2005; Storey et al., 2007a; Frieling et al., 2016; Saunders, 2016; Gutjahr et al., 2017). To refine this relationship, better constraints on the relative timings of volcanic activity and climatic and environmental changes are needed.

In our previous paper from Stolleklint, we presented a high resolution sea surface temperature (SST) reconstruction based on the organic palaeothermometer TEX₈₆ (Stokke et al., 2020a). We found that SSTs increased by about 10 °C across the CIE onset, and then gradually decreased during the CIE body and recovery (Fig. 2; Stokke et al., 2020a). Here, we combine mineralogical, sedimentological, and geochemical proxies to investigate the relationship between changes in temperature and variations in both basin oxygenation and sediment input; the latter typically inferred to indicate changes in terrestrial erosion and runoff. Both increased weathering of siliciclastic rocks and enhanced sequestration of organic carbon have been proposed as important negative feedback mechanisms, potentially driving the PETM recovery (Speijler and Wagner, 2002; Bowen and Zachos, 2010; Ma et al., 2014; Penman, 2016; Dunkley-Jones et al., 2018). Better constraints on the timing and global extent of increased silicate weathering and organic matter sequestration drawdown are therefore vital for understanding the PETM termination.

2. Field area and stratigraphy

Stolleklint is located on the northern shore of the island of Fur in northwest Denmark (Fig. 1). In the Palaeogene, Fur was part of the Norwegian–Danish Basin, a marginal basin in the eastern semi-enclosed epicontinental North Sea Basin (Rasmussen et al., 2008; Knox et al., 2010). The Norwegian–Danish Basin forms a NW to SE striking depression, bounded by the Fennoscandian Shield and the Sorgenfrei–Tornquist Zone to the NE and basement blocks in the Ringkøbing–Fyn High to the SW (Schiøler et al., 2007). Salt diapirs of Zechsten salt creates additional restricting structures within the Norwegian–Danish Basin (e.g. Petersen et al., 2008).

The base of the section at Stolleklint likely comprises the Holmehus Formation, which correspond to the Lista Formation offshore in the North Sea (Figs. 2, 3, 4). This is a hemipelagic bioturbated fine-grained mudstone, representing the culmination of a long period of transgression in the latest Paleocene Denmark (Heilmann-Clausen, 1995). In the latest Paleocene, a combination of thermal uplift around the NAIP (Knox, 1996) and tectonic uplift along the Sorgenfrei–Tornquist Zone (Clausen et al., 2000) led to a relative sea-level fall and almost complete isolation of the North Sea Basin (Knox et al., 2010). In Denmark, this resulted in either erosion of the latest Paleocene strata, a hiatus in deposition, or deposition of the informal Østerrende clay unit above the Holmehus Formation. However, the Østerrende clay unit has a very limited regional distribution, and it is uncertain how much

is present at Stolleklint despite its presence further south in Denmark (Fig. 2; Schmitz et al., 2004; King, 2016). Schoon et al. (2015) correlated the uppermost Paleocene stratigraphy at Fur with the Østerrende clay similar to that seen at Store Bælt (Fig. 1a). However, the Østerrende clay is absent in cores drilled at Mors ~20 km to the west and at Ølst ~80 km to the SE (Fig. 1aA; Heilmann-Clausen, 1995), suggesting that a hiatus of uncertain duration followed the Holmehus Formation at Stolleklint. Still, due to the uncertainty of this boundary, we will henceforth refer to the lowermost unit as the Holmehus/Østerrende Formation.

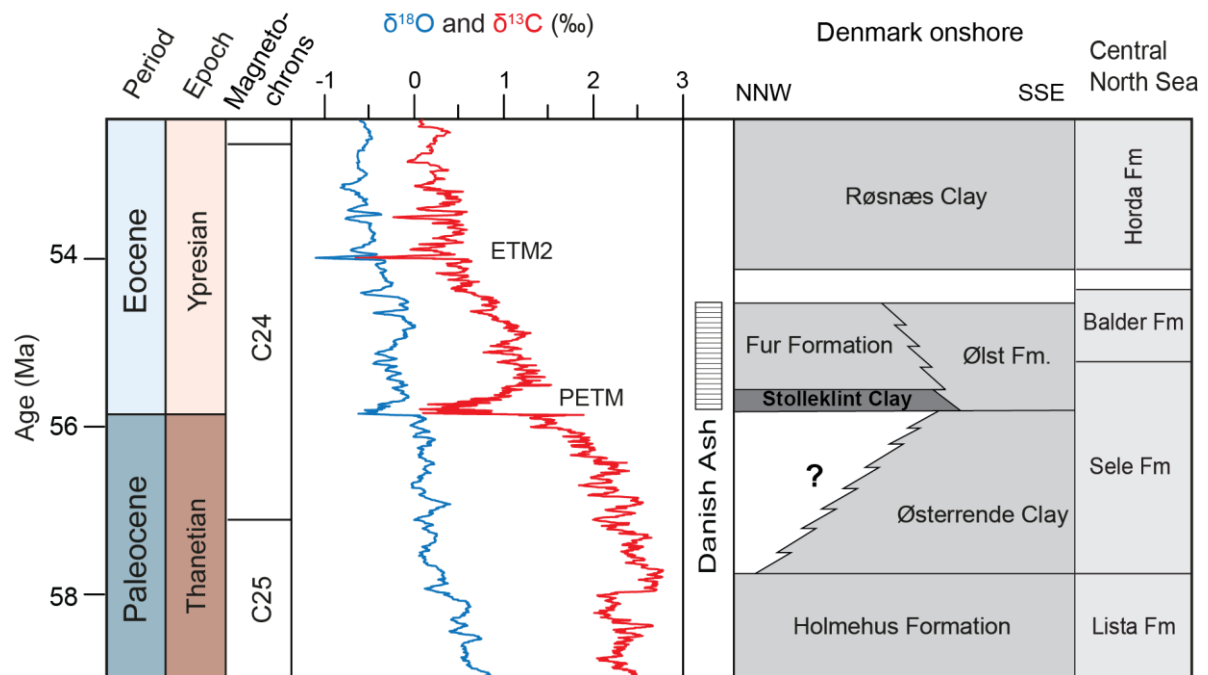


Figure 2: Composite figure of the late Paleocene and early Eocene interval, indicating both the Danish stratigraphy and the correlative offshore North Sea stratigraphy. Stratigraphy from King (2016) and Schiøler et al. (2007). The $\delta^{13}\text{C}$ and $\delta^{18}\text{O}$ curves indicate the stratigraphic position of two periods of carbon perturbation; the Paleocene–Eocene Thermal Maximum (PETM) and the Eocene Thermal Maximum 2 (ETM2). Carbon and oxygen isotope data from Cramer et al. (2009) and Littler et al. (2014) and plotted on the GTS2012 timescale (Ogg, 2012).

The Paleocene–Eocene transition is seen as a lithological shift from the Holmehus/Østerrende Formation bioturbated clays, into the dark, laminated clays of the Stolleklint Clay (Figs. 3, 4; Heilmann-Clausen et al., 1985; Heilmann-Clausen, 1995; King, 2016). The lithological shift is accompanied by the almost complete absence of benthic fauna and preferential dissolution of remaining calcareous organisms within the Stolleklint Clay (Heilmann-Clausen, 1995; Mitlehner, 1996). The Stolleklint Clay is an informal unit, representing the lower Ølst Formation in northern Denmark and correlating with the offshore Sele Formation (Fig. 2; Heilmann-Clausen, 1995). A condensed, glauconite-rich silty horizon marks the Stolleklint Clay base (Heilmann-Clausen, 1995, Schmitz et al., 2004; Schoon et al., 2015). This glauconite-rich silt contains mainly authigenic and biogenic grains and was likely deposited in an upper bathyal to outer neritic environment with low sedimentation rates (Nielsen et al., 1986; Schoon et al., 2015). A relative sea level rise is recorded in PETM sections in the Atlantic, Pacific, Tethyan, and Arctic Oceans (Sluijs et al., 2008; Harding et al., 2011; Pujalte et al., 2014; Sluijs et al., 2014). It was likely caused by thermal expansion of seawater due to global warming (Sluijs et al., 2008), and may pre-date the PETM up to 20–200 kyr (John et al., 2012). Although this transgression was overprinted by regional tectonically forced regression in the latest Paleocene, the earliest Eocene Stolleklint Clay is deposited in an outer neritic

environment (between 100–200 m; Knox et al., 2010; Schoon et al., 2015) during a gradual transgression (Heilmann-Clausen, 1995). The Stolleklint Clay is overlain by the ~60 m thick clay-rich Fur Formation diatomites (Figs. 3, 4), correlating to the offshore Sele and Balder Formations (Fig. 2). At Stolleklint, the PETM is defined by a negative CIE of -4.5 ‰ based on stable carbon isotopes of bulk samples ($\delta^{13}\text{C}_{\text{TOC}}$). The CIE is characterized by a sharp (2cm) onset above Ash SK2 at the base of the Stolleklint Clay, a thick stable body phase (~24 m), and a gradual recovery (~4.5 m) from about Ash -33 to around Ash -21a (Fig. 3, 4; Jones et al., 2019). Recent glaciotectonic activity has resulted in a relatively steep bedding with internal small scale folding and thrusting (Pedersen, 2008), complicating stratigraphic thickness estimates. Jones et al. (2019) used trigonometry to estimate a local true thickness of 24.4 ± 2 m (24.2 m excluding ash layers) for the PETM onset and body at the Stolleklint beach; from the top of Ash SK2 to the base of Ash -33 within the excavated trench. An overall sedimentation rate was then calculated for the PETM body based on the estimated true thickness and an assumed 100 kyr duration for the PETM body (van de Meulen et al., 2020). The PETM at Stolleklint is consequently associated with a substantially increased sedimentation rate from the condensed glauconitic base to a maximum sediment accumulation rate in the Stolleklint Clay of about 24 cm/kyr (Stokke et al., 2020a).

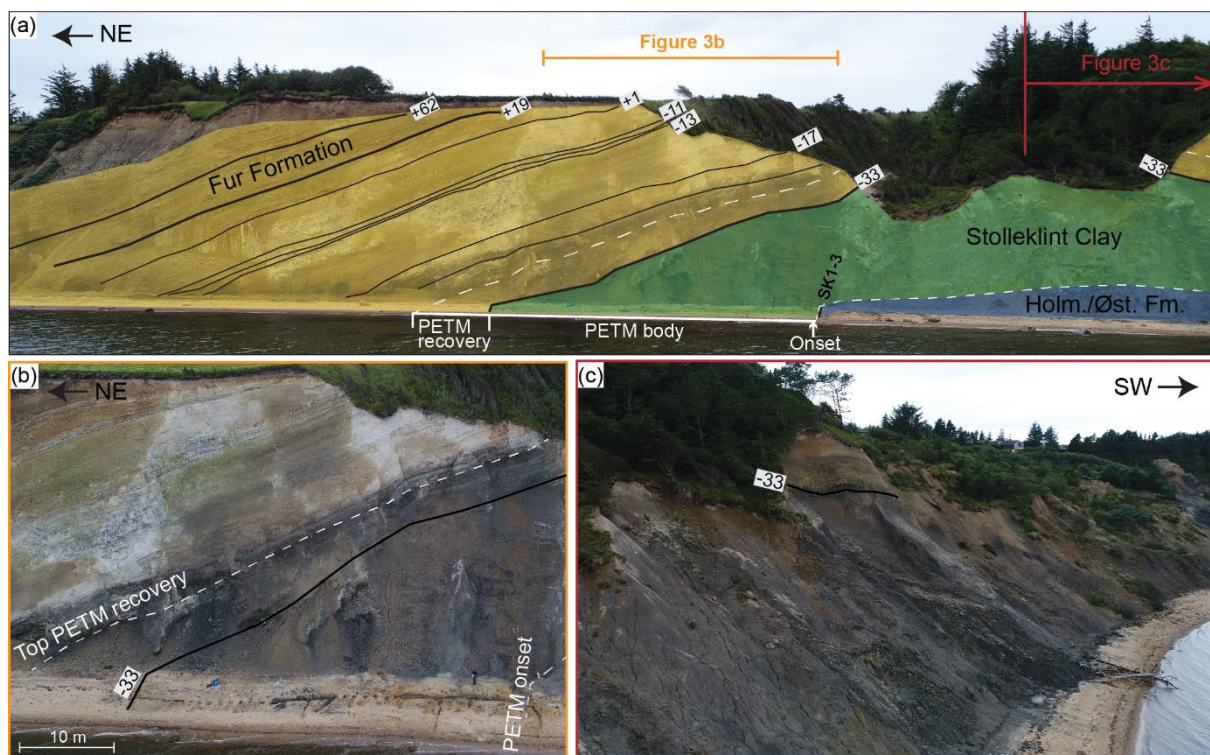


Figure 3: a) Picture of the coastal cliff at the Stolleklint beach with the main stratigraphic units shown as yellow (Fur Formation), green (Stolleklint Clay), and blue (Holmehus/Østerrende Formation). The black lines indicate certain key ash layers, and white dashed lines indicate the upper and lower bounds of the PETM CIE. b) Close up of the central part of the cliff face showing the colour difference between the dark PETM clays and the light post-PETM diatomites. Ash -33 and the PETM CIE are indicated. Note the 43 m long ditch on the beach where most of the samples were collected. c) Picture of the continued cliff side towards the west, showing the extensive coastal erosion. Approximate location of Ash -33 is indicated.

More than 180 tephra with thicknesses up to 20 cm have been identified in the stratigraphy exposed at Fur, with the majority (~140) within the post-PETM Fur Formation (Fig. 2; Bøggild, 1918; Pedersen and Surlyk, 1983). Tephra is a general term for all air-borne volcanic fragmented material, but the grain sizes of all the Fur tephra

are <2 mm and therefore within the ash fraction. Heavily altered ashes are called bentonites, and while this applies to some of the lowermost ashes we will for simplicity use the term ash for all. The volcanic ashes are grouped in a negative and positive ash series based on variations on outcrop appearance and geochemistry (Bøggild, 1918), with additional ash layers SK1–4 identified later at the base of the Stolleklint Clay (Schmitz et al., 2004; Jones et al., 2019). The SK ashes and the negative series are a heterogeneous mix of ash compositions, whereas the positive series are largely comprised of tholeiitic basalts (Morton and Evans, 1988; Larsen et al., 2003). All the ashes are believed to be sourced from NAIP explosive volcanism during the northeast Atlantic opening (Larsen et al., 2003; Storey et al., 2007a; Stokke et al., 2020b). These ash layers are found throughout the North Sea and North Atlantic (Knox and Morton, 1988; Haaland et al., 2000) with some of the major layers traced all the way to Austria, suggesting that ash was occasionally distributed all over Northern Europe (Egger et al., 2000).

3. Materials and methods

3.1 Sampling

Samples were mostly collected from the Stolleklint beach (56°50'29''N, 8°59'33''E; Figs. 1B, 3), with some additional samples from a quarry near Fur Camping (Quarry FQ16 at 56°49'51''N, 8°58'45''E; Fig 1B). At Stolleklint, the Stolleklint Clay and the Fur Formation are exposed in the cliff side (Fig. 3). However, the base of the Stolleklint Clay and the Paleocene–Eocene transition were not exposed at the time of field work due to coastal erosion (Fig. 3C). We therefore excavated a 43 m long and 0.5 m deep trench along the beach (Fig. 4B). ~~Recent glaciotectonic activity has resulted in a relatively steep bedding with internal small scale folding and thrusting (Pedersen, 2008), complicating stratigraphic thickness estimates. Jones et al. (2019) used trigonometry to estimate a local true thickness of 24.4 ± 2 m (24.2 m excluding ash layers) for the PETM onset and body at the Stolleklint beach; from the top of Ash SK2 to the base of Ash -33 within the excavated trench. This estimated true thickness of 24.4 m from the top of Ash SK2 to the base of Ash -33 is used as the depth scale for stratigraphic presentation (e.g. Fig. 4). The scale is measured as positive and negative depth relative to the base of the main marker bed Ash -33. As the PETM was the main target, samples are collected at highest resolution across the PETM onset, then at lower resolution within the PETM interval and in the post-PETM section: Discrete 1 cm-thick samples were collected at 1 cm intervals (i.e. 100% sampling) from ~25 cm below to ~90 cm above Ash SK1, (in estimated true thickness), and then at 0.5 m intervals (0.2-0.3 m when converted to the estimated true thickness) up to Ash -33. Samples above ash -33 were collected from the cliff face at Stolleklint at ~10–20 cm intervals. Additional samples from -5.6 to +1.9 m relative to the base of Ash -33 were included from the quarry FQ16, sampled at ~30 cm intervals. All samples were oven dried at ≤50 °C and powdered in an agate hand mortar or an agate disc mill before further analysis.~~

The sediments' unconsolidated character enabled the collection of 4 box-cores up section. The box-cores were collected in 50 cm long, and 5 cm wide and deep aluminium boxes. These were pushed into the sediments before surrounding material was removed and the box cut away with its content intact using a steel wire. Box-cores were collected in order to get complete recovery of selected intervals for XRF core scanning (Fig. 4). Two box-cores were collected across the PETM onset (-24.90 to -24.40 m and -24.63 to -24.20 m stratigraphic depth intervals), and two from the PETM body with one from the lower laminated part (-14.47 to -14.17 m) and one from the non-laminated upper part (-10.81 to -10.48 m).

3.2 XRD bulk and clay mineralogy

240 Bulk rock mineralogy was conducted on 8 samples from -24.81 to +5.35 m depth, while 13 samples were analysed for clay minerals. The mineralogy of both bulk rock and clay fraction ($< 2 \mu\text{m}$) of Fur sediment samples were determined by X-ray diffraction (XRD) analyses on a Bruker D8 ADVANCE diffractometer with a Lynxeye 1-dimensional position-sensitive detector (PSD) and $\text{CuK}\alpha$ radiation ($\lambda = 0.154 \text{ nm}$; 40mA and 40kV) at the Department of Geosciences, University of Oslo. The bulk-rock fraction was wet milled in a McCrone Micronizing
245 Mill, prepared as randomly oriented samples, and analysed with a step size of 0.01° from 2° to 65° (2θ) at a count time of 0.3 s (2θ). The software DIFFRAC-EVA (v. 2.0) was used for phase determination, and phase quantities were determined by Rietveld refinement (Rietveld, 1969) using PROFEX (v. 3.13.0; Doebelin and Kleeberg, 2015).

The clay fraction ($< 2 \mu\text{m}$) was separated from the crushed whole-rock sample (before wet milling) by gravity
250 settling, and then prepared as oriented aggregate mounts using the Millipore filter transfer method (Moore and Reynolds, 1997). As the dried samples had to be powdered prior to separation, they contain some minor contribution from the coarser fraction. XRD clay data were recorded with a step size of 0.01° from 2° to 65° (2θ) at a count time of 0.3s (2θ) in air-dried samples, and a step size of 0.01° from 2° to 34° (2θ) at a count time of 0.3s (2θ) on treated samples. Three rounds of treatments were applied: 24h of ethylene glycol saturation, 1h heating at
255 350°C , and 1h heating at 550°C . The software NewMod II (Reynolds and Reynolds, 2012) was used for semi-quantification of the XRD-patterns of inter-stratified clay minerals.

3.3 XRF elemental core scanning

Non-destructive geochemical measurements and radiographic images were obtained from the box-cores with an
ITRAX X-ray fluorescence (XRF) Core Scanner (Croudace et al., 2006) from Cox Analytical Systems at the
260 EARTHLAB facilities, Department of Earth Science, University of Bergen. The core scanner was fitted with a molybdenum X-ray tube run with power settings at 30 kV and 30 mA. The box-cores were scanned with 10 s exposure time at 0.5 mm sampling intervals.

3.4 Rock-Eval pyrolysis

A total of 39 samples were analysed between -24.81 and +0.01 m depth. Analyses were conducted at the University of Oxford on a Rock-Eval 6 (Vinci Technologies SA, Nanterre, France; Behar et al., 2001) with pyrolysis and oxidation ovens, a flame ionization detector, and infra-red cell. Powder aliquots of 50 mg were weighed into crucibles and heated first at a temperature profile of $300 - 650^\circ\text{C}$ in a pyrolysis furnace and then at $300-850^\circ\text{C}$ in an oxidation oven. For a detailed methodology on the Rock-Eval 6 application, see Lafargue et al. (1998).

The bulk organic-carbon characteristics including the hydrogen index (HI), oxygen index (OI), and T_{max} were investigated using RockEval data. The HI (expressed as mg HC/g TOC) corresponds to the quantity of hydrocarbons per gram TOC, and the OI (expressed as mg CO_2 /g TOC) to the quantity of oxygen released as CO and CO_2 per gram TOC. Sediment records of HI and OI provide information on both organic matter sources and processing. The HI typically reflect the relative distribution of terrestrially and marine derived organic matter, while the OI index indicate the degree of oxidation of the organic matter. The ratio of HI/OI can be used to indicate
270 the degree of organic matter alteration. A HI/OI < 1 in sediments typically indicate a high degree of alteration, while fresh organic matter has a HI/OI > 2 as oxid degradation preferentially removes hydrogen-rich compounds

(Hare et al., 2014). T_{max} is the temperature at which the maximum amount of S2 hydrocarbons are generated. It can be used to indicate the degree of organic matter maturation with T_{max} temperatures <435 °C typically indicating immature organic matter (Peters, 1986).

The bulk organic carbon characteristics including the hydrogen index (HI), oxygen index (OI), and T_{MAX} were determined by analysing ca 50 mg powder aliquots with a Rock Eval 6 (Vinci Technologies SA, Nanterre, France; Behar et al., 2001) at the University of Oxford. A total of 39 samples were analysed between -24.81 and +0.01 m depth. The HI corresponds to the quantity of hydrocarbons per gram TOC, and reflects the relative distribution of terrestrially and marine derived organic matter. A HI <100 indicates a dominantly terrigenous source, while a HI >>100 indicates the presence of significant amount of aquatic algae (marine and/or freshwater) and/or microbial biomass (e.g. Stein et al., 2006).

3.5 ICP-MS and Element Analyser

Analyses were conducted on 24 samples between -24.82 to +5.50 m depth. Dried and crushed marine sediment samples were digested in hydrochloric, hydrofluoric, and nitric acids to give a total dilution of $\sim 4 \times 10^6$ -fold by volume. Major and trace element analyses of digested bulk sediment samples were performed on a PerkinElmer NexION 350D ICP-MS. Total sulfur concentrations were analysed on a Coulomat 702 coulometric analyser. Sample digestion and analyses were all conducted at the Department of Earth Sciences, University of Oxford. The method detection limit, accuracy, and precision of the analyses are given indicated in the supplementary material (Table 4, Supplement 1). Major elements analysed on ICP-MS were converted from elemental mass units to oxide wt% equivalents. The trace metals Cu, Ni, Mo, U, and V were calculated as enrichment factors (Eq. 1) to account for possible dilution using standard Al values of average upper crust from McLennan (2001).

$$EF_{element\ X} = \frac{X}{Al_{sample}} / \frac{X}{Al_{standard}} \quad (1)$$

P_2O_5 , Ba, Cu, Ni, and V have all been normalized to Al_2O_3 to account for the potential detrital influx, as Al_2O_3 indicates the aluminosilicate fraction of the sediments (Tribouillard et al., 2006).

ICP-MS analyses of major elements were used to calculate the chemical index of alteration (CIA; Nesbitt and Young, 1982). The CIA is a measure of weathering intensity based on the relative distribution of mobile cations relative to aluminium oxide, and indicates the extent of conversion of feldspars (which dominate the upper crust) to clays such as kaolinite (Nesbitt and Young, 1982). While the CIA may directly represent the rate and intensity of weathering when measured *in situ*, when measured in marine sediments it becomes more complex as it also reflects changes in the type of sediment sources and the transport sorting processes (Eq. 2; Nesbitt and Young, 1982). The CIA is expressed as:

$$CIA = \left(\frac{Al_2O_3}{Al_2O_3 + CaO^* + K_2O + Na_2O} \right) * 100 \quad (2)$$

Where Al_2O_5 , CaO^* , K_2O , and Na_2O are given as whole-rock molecular proportions, and CaO^* is the total silicate fraction of CaO corrected for the presence of carbonates and phosphates following the approach of McLennan, 1993. First, apatite was accounted for using the molecular proportions:

$$CaO^{ap} = CaO - \left(\frac{10}{3} * P_2O_5 \right) \quad (3)$$

As we do not have measurements of CaCO_3 from the source rock, we assume a ratio of $\text{Ca}/\text{Na}=1$ (McLennan, 1993), and that samples with excess CaO is where $\text{CaO}^{\text{ap}} > \text{Na}_2\text{O}$. We then find that $\text{CaO}^* = \text{Na}_2\text{O}$ where $\text{CaO}^{\text{ap}} > \text{Na}_2\text{O}$ and $\text{CaO}^* = \text{CaO}^{\text{ap}}$ where $\text{CaO}^{\text{ap}} \leq \text{Na}_2\text{O}$.

315 **4. Results**

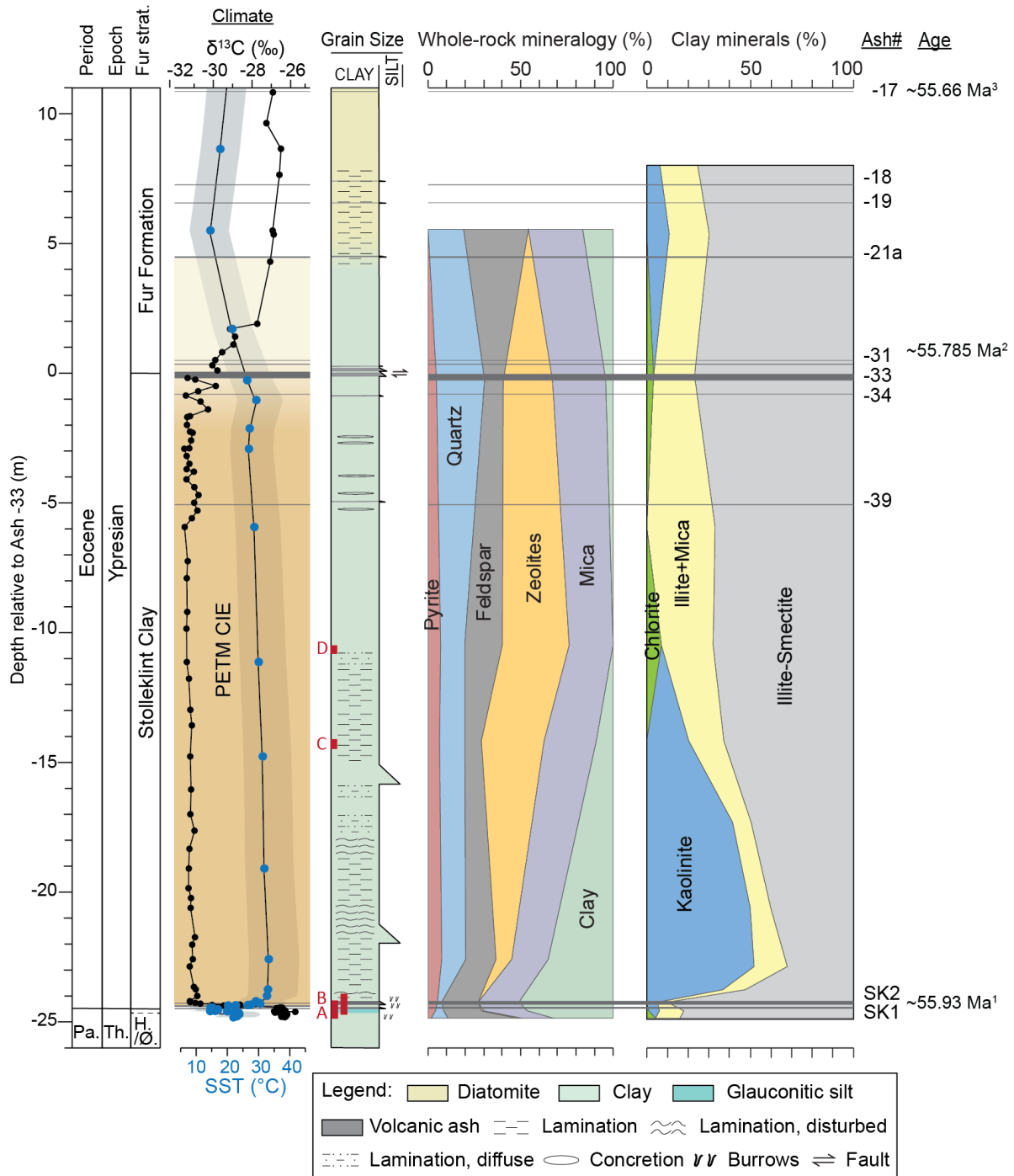


Figure 4: The studied stratigraphy from the island of Fur shown to the left with the depth scale measured upwards and downwards from the main marker bed Ash -33. Strat. = stratigraphy, Pa. = Paleocene, Th. = Thanetian, H./Ø. = Holmehus/Østerrende Formation (dotted line indicate base of the glauconitic silt). Overall climate indicated based on previously published data from the study area. The yellow column indicates the interpreted PETM CIE duration, based on the $\delta^{13}\text{C}$ curve

320

from Jones et al. (2019). The base of the column marks the CIE onset, and the gradually lighter colours toward the top marks the CIE recovery. Sea surface temperature (SST) variations are given as BAYSPAR calibrated TEX_{86} SSTs with 1σ error bar indicated by the light blue area (Stokke et al., 2020a). Sedimentological log from Stolleklint with legend below. Red squares labelled A–D indicate the stratigraphic position of XRF box-core scans position shown—in Figures 56 and 6. Bulk-rock and clay mineralogy is presented as percentage. $\delta^{13}\text{C}$ data from Jones et al. (2019), TEX_{86} data from Stokke et al. (2020a). Ages indicated to the right are based on ¹Westerhold et al., 2018; ²Charles et al. (2011), assuming the Svalbard and Fur CIEs timing is coeval; ³ Corrected Ar-Ar age of Ash -17 from Storey et al. (2007a) recalibrated to the FCT calibration from Renne et al. (2010; 2011) to 55.66 ± 0.12 Ma.

4.1 Sedimentology

The base of the beach section comprises the Holmehus/Østerrende Formation (Figs. 3, 4), which is composed of dark, blueish clay with pervasive bioturbation. It is overlain by a greenish silty layer indicative of glauconite (marked with G in Fig. 5), with up to coarse sand-sized aggregates of glauconite scattered within the clay. The silts lower boundary is unclear, but it appears conformable and possibly gradational. The 5 cm thick ash layer SK1 is deposited above the glauconitic silt, with a sharp undulating lower boundary (Fig. 5). About 4.5 cm of structureless, grey clay conformably overlies SK1, and is followed by the ~8 cm thick ash layer SK2 (Fig. 5). Both ashes are light grey and seems to be heavily altered. They are upward fining from medium sand to clay-sized particles. Both ashes are relatively reworked and become gradually more clay-rich toward the top, with the highest bioturbation intensity at the top of Ash SK2 (Fig. 5). About 2 cm of strongly bioturbated and ash-rich clay overlying the ash is abruptly ended by the initiation of dark laminations (Fig. 5 section B). The exact level of the Stolleklint Clay base is uncertain as the boundary is blurred by ashes SK1 and SK2, but the start of the laminations is included in the Stolleklint Clay, placing the boundary no higher than here (Fig. 5 section B). Laminated dark clay continues for ~10 cm before deposition of two ash layers SK3 and SK4, ~1 cm and ~0.4 cm thick respectively (Fig. 5 section B). They are separated by 2 cm of clay with slightly undulating lamination. Above the ash, laminated clay continues about half-way up the beach (Fig. 4), with increasingly folded and disturbed layering (Fig. 6 section C).

The PETM body is dominated by hemipelagic clay. Above the lower laminated part, it appears to have an upper part (from about -10 m depth) comprising very dark grey clay with no visible laminations in field exposures (Fig. 4). However, the XRF radiographic image reveals that there are intermittent diffuse laminations and patchy structures/colour differences within the clay (Fig. 6 section D). The cause of these colour patches is uncertain, but could be a result of depositional variations and/or post-depositional deformation. Between about -6 and -2 m depth there are some highly pyritized concretions, or likely broken up concreted layers (Fig. 4). Ash layers reappear from about -5 m depth with deposition of the thin (~2 cm), black Ash -39 (Fig. 4). Ashes -34, -33, -32, and -31 are deposited relatively closely spaced between -0.85 to +0.05 m depth, with thicknesses of 2, 20, 2 and 3 cm respectively. The thickest layer Ash -33 is repeated at the Stolleklint Beach, due to a small glaciotectonic thrust fault (Fig. 4). The boundary between the Stolleklint Clay and the Fur Formation is formally placed at Ash -33, although there is no sharp lithological boundary (Figs. 3, 4). Dark clays continue upward with a gradually increasing diatomite content. Laminations re-appear at about +6 m depth, as the lithology become dominated by clay-rich diatomite (Fig. 4).

4.2 Mineralogy

360 The bulk mineralogy comprises six main phases: zeolites, mica, clay (including smectite, chlorite, kaolin minerals, and glauconite), feldspars, quartz, and pyrite (Fig. 4). Phyllosilicates dominate the bulk mineralogy in the lower laminated part of the stratigraphy. While the mica fraction remains relatively stable throughout, the clay fraction reaches its maximum of 50.6 % at ~13 cm above Ash SK2 and the CIE onset (-24.24 m depth), before decreasing substantially upward from about -22 m depth to nearly 0 % at -10 m depth (Fig. 4). Zeolites (of the heulandite–clinoptilolite type) dominate the CIE body, comprising up to 36 % of the bulk mineralogy at -10.48 m depth (Fig. 365 4). The fraction of feldspars is largest within the Holmehus/Østerende Formation (37 % at -24.81 m depth) and during the CIE recovery (35 % at +5.35 m depth), while quartz increases in the upper part of the stratigraphy up to 26 % at -0.28 m depth (Fig. 4). Pyrite makes up the smallest fraction of the bulk mineralogy (Fig. 4). It increases from 1.9 % in the lower Holmehus/Østerende Formation (-24.81 m depth) to 5.3 % ~13 cm above the CIE onset (-24.24 m depth). The highest fraction of pyrite (6.1–7.5 %) is reached during the CIE body, before values decrease 370 during the PETM recovery to a minimum of 0.11 % at +5.35 m depth.

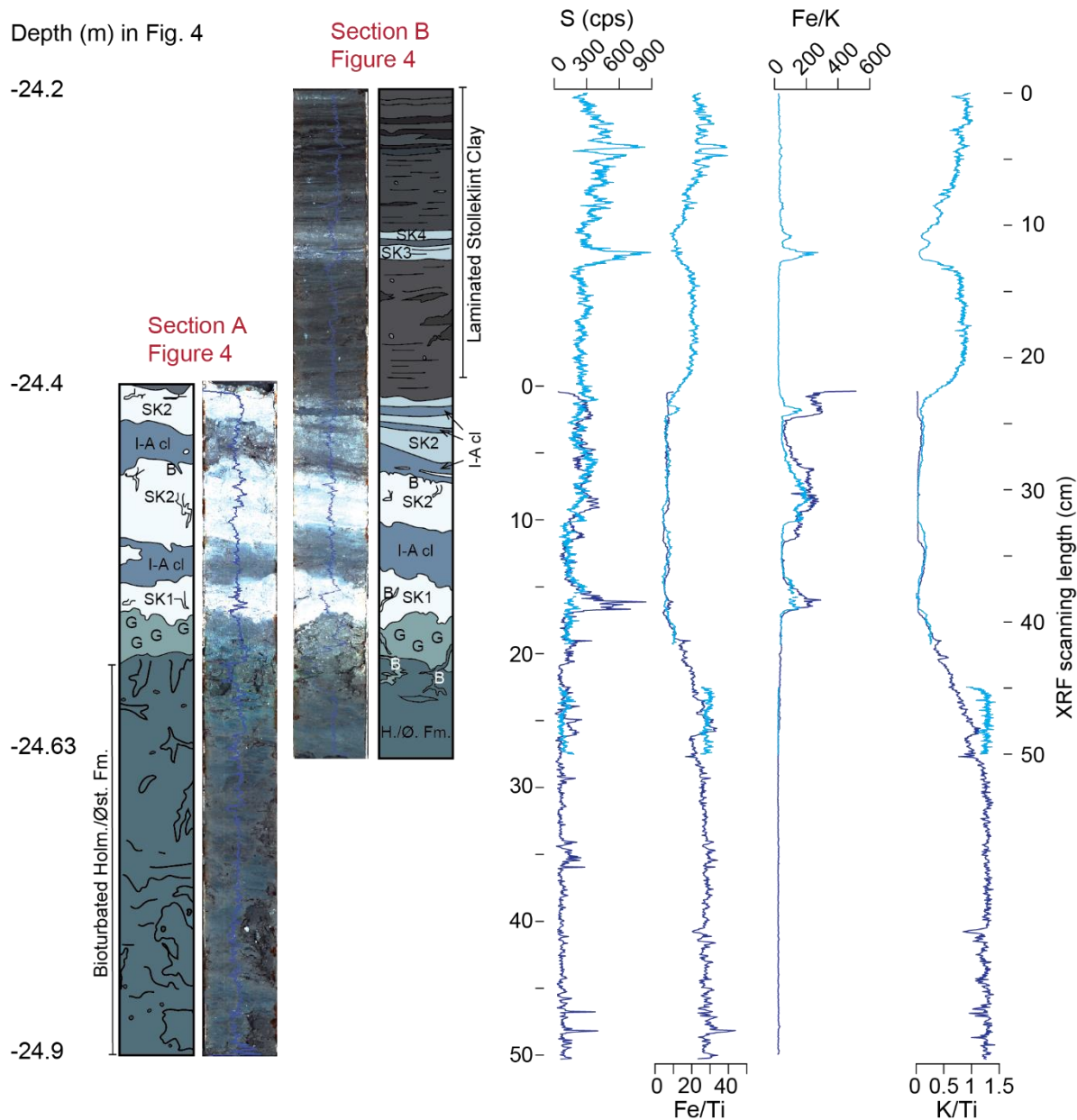


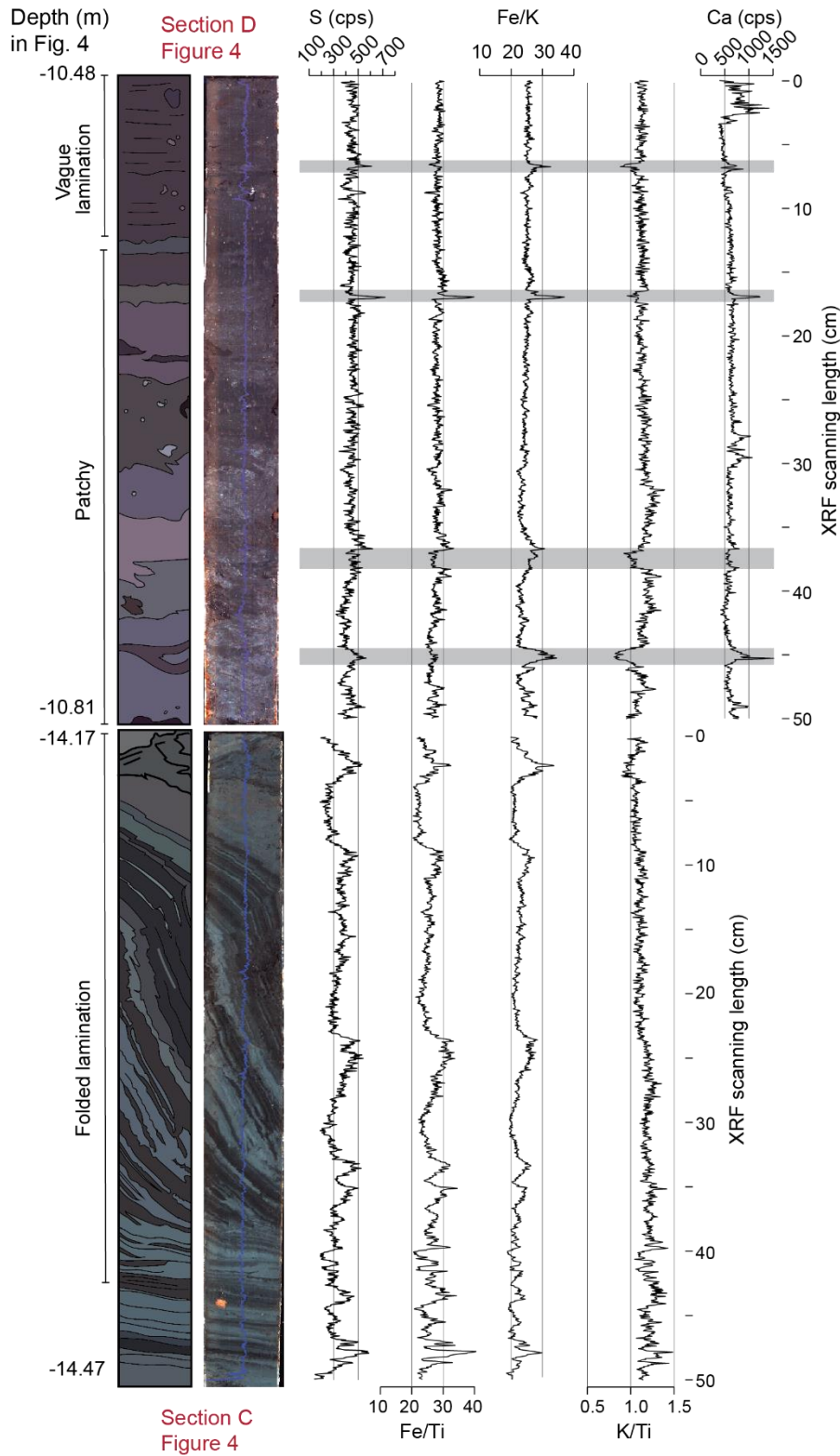
Figure 5: XRF element core scans and radiographic images of two box-cores crossing the PETM onset at the Stollekint beach. Note that despite some cracks in the surface below Ash SK1, the sample preservation is overall good and XRF core scanning were conducted on a smoothed surface along the centre avoiding any substantial irregularities. Interpretive logs next to the images indicate the lithological changes. G=Glaucanite; B=Burrow; I-A cl=Inter-ash clay. The corrected stratigraphic depth relative to Ash -33 of each section is indicated to the left. XRF scanning length seen to the right indicate actual box-core length. XRF data given as counts per second (cps) or as dimensionless ratios.

375

380

Clay fraction XRD analyses identified four major clay mineral phases: kaolinite, chlorite, mixed-layer illite-smectite with only minor illite layers indicating almost pure smectite, and illite + fine-grained mica (Fig. 4). Illite-smectite is the dominating clay mineral within the studied section. It comprises 84–90 % of the total clay from the base and up to 13 cm above the CIE onset (-24.24 m depth), before decreasing in the lower PETM body to a minimum of 32 % about 1.5 m above the CIE onset (-22.86 m depth). The illite-smectite content increases throughout the upper CIE body and recovery with values between 50–77 % (Fig. 4). Illite + fine-grained mica comprises a smaller part of the total clay fraction, with 10 % during the CIE onset, and a maximum of 33 % at -

385 5.93 m depth (Fig. 4). Kaolinite increases substantially from 5 % about 13 cm above the CIE onset (-24.24 m depth) to 37 % at 62 cm above the CIE onset (-23.75 m depth). Kaolinite dominates the clay fraction in the lower laminated PETM body with a maximum of 52 % at -20.60 m depth, before disappearing in the upper PETM body and re-emerging with 11 % during the recovery phase (+5.35 m depth; Fig. 4). Chlorite only appear in 4 of 13 samples and makes up the smallest part of the clay fraction, with a maximum of 7 % at -10.48 m depth (Fig. 4).



390

Figure 6: XRF element core scans and radiographic images of two box-cores within the PETM body from the Stolleklint beach. The sample preservation of these box-cores were excellent with no substantial irregularities. Interpretive logs next to the images indicate the lithological changes. The corrected stratigraphic depth relative to Ash -33 for each section is indicated to the left, while the XRF scanning length to the right indicate actual box-core length. Grey bands in section D indicate potentially tephra-rich horizons. XRF data given as counts per second (cps) or as dimensionless ratios.

4.3 XRF core scanning Box-core major element variations

Two box-cores cross the PETM onset, covering the transition from Holmehus/Østerrende Formation into Stolleklint Clay, and the ash layers SK1–SK4 (Figs. 4, 5, 6). ~~Sulfur counts show a slight overall increase from below to above the ashes, suggesting gradually more suboxic conditions above the ashes.~~ Low K/Ti and Fe/Ti ratios suggest that the ashes are Ti-rich basalts. The gradual decrease in both K/Ti and Fe/Ti below Ash SK1 may subsequently suggests a potential gradual increase in volcanic-derived material before the first ash layers in the Danish Basin appears (Fig. 5). ~~Sulfur counts show a slight overall increase from below to above the ashes. Peaks in S counts indicate particularly S rich parts of the ashes, although when correlating with Fe/Ti peaks it is more likely due to suboxic formation.~~ Above Ash SK3, there are several peaks of S, Fe/Ti, and Fe/K (although the latter signal is swamped by the iron-rich ashes in Fig. 5 section B) that correlate with each other and with the dark laminations, ~~suggesting at least periods of decreased oxicity.~~

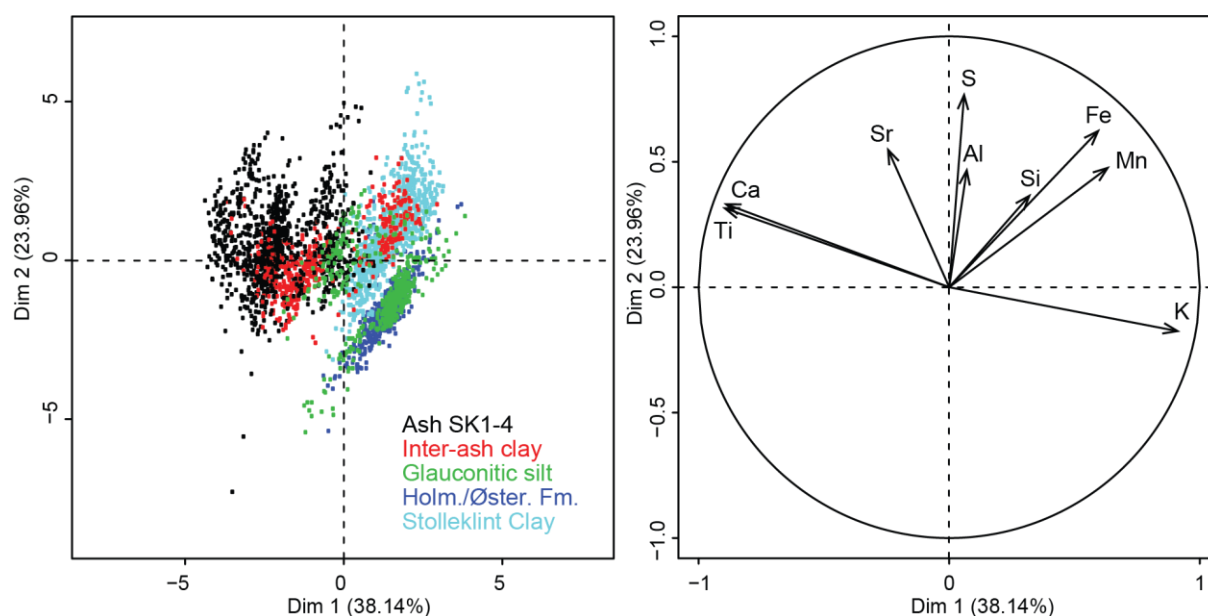
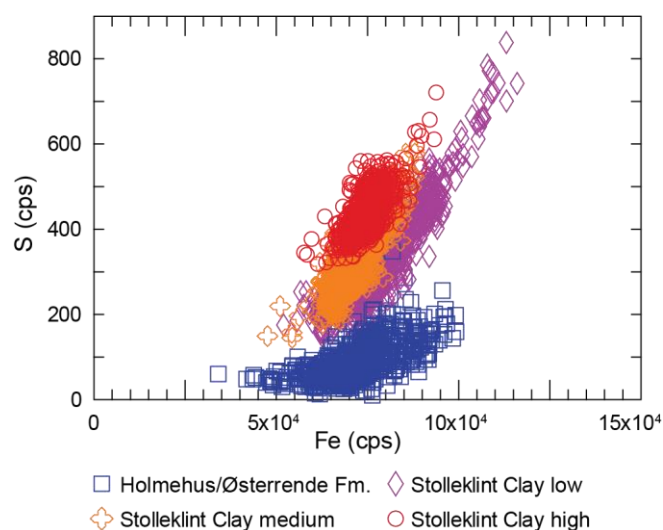


Figure 7: Biplot (left) and correlation circle (right) with Dimensions 1 and 2 (denoted as Dim 1 and Dim 2) of the principal component analysis applied to XRF core scanning data from box cores 1 and 2 across the PETM onset. Dimensions 1 and 2 represent 62 % of the total variability. The inter-ash clay in the Biplot refers to the clay between ashes SK1 and SK2 as indicated in Figure 5.

Principal component analysis reveal a distinct difference in chemistry between the Holmehus/Østerrende Formation and the Stolleklint Clay (Fig. 7). It also indicates that both the clay between ashes SK1 and SK2 and parts of the glauconitic silt likely include a large ash component. While the glauconitic silt is chemically closer to the underlying Holmehus/Østerrende Formation than the Stolleklint Clay, the less ash-rich inter-ash clay appears to have a composition closest to the Stolleklint Clay. This suggests that this is indeed a part of the Stolleklint Clay base, and we therefore propose that Ash SK1 marks the lower Stolleklint Clay boundary. The correlation circle

indicate that differences in Ca and Ti on one hand and K on the other is the main controlling factors, reflecting the variation between volcanic and clay dominated fractions respectively (Fig. 7).



420

Figure 8: Biplot of Fe and S. Data from XRF element core scans of all four box-cores. CPS = Counts Per Second.

The box core in Figure 6 section C, covering the lower Stolleklint Clay, shows that the sediments are strongly laminated and slightly folded. Elevated S concentrations and high Fe/Ti and Fe/K ratios indicate anoxic conditions. Correlations between these peaks in anoxia and dark laminations (Fig. 6 section C) suggesting that there were some regular variability in basin oxygenation in bottom-water oxieity. The K/Ti ratio remains relatively stable, suggesting no dramatic lithological changes. Figure 6 section D shows the non-laminated upper Stolleklint Clay, which displays relatively minor elemental variations. However, drops in the K/Ti ratio could indicate areas of increased volcanically-derived material, potentially as cryptotephra (Fig. 6 section D); defined as volcanic tephra deposits not visible to the naked eye. The presence of cryptotephra layers is particularly likely when low K/Ti ratios correlate with increases in Fe/Ti and Ca, and to some extent S. Relative changes in Fe/Ti and to some extent Ca depend strongly on the source of the volcanic material. The biplot of S and Fe (Fig. 8) shows that there is an overall increase in S upward from the pre-PETM Holmehus/Østerrende Formation and throughout the Stolleklint Clay. It also indicate that there upper PETM body have a more homogenous high sulfur content, while there is significant variation in the sulfur counts between dark and light laminations in the lower laminated PETM body, as also observed in the XRF core scans (Fig.8 section C). shows that the variability of S measurements decreases upward, and that there is an overall increase in S upward from the pre-PETM Holmehus/Østerrende Formation and throughout the Stolleklint Clay.

425

430

435

4.4 Organic geochemistry

The thermal immaturity of the Stolleklint Clay has previously been suggested based on the dominating odd over even preference in long-chained n-alkanes (Stokke et al., 2020a). This is now also verified by the low RockEval T_{max} values of <422 °C (Table 3, Supplement 1). The HI peaks up to 150 mgHC/gTOC in the glauconitic silt between -24.61 to -24.59 m depth, but is otherwise <100 mgHC/gTOC pre-PETM (Fig. 9). The HI increases >100 mgHC/gTOC about 13 cm above the CIE onset at -24.05 m depth. A second major increase in HI occurs above -14 m depth, after which values remain high and reaches maximum values of 303 mgHC/gTOC at -0.78 m depth (Fig. 10). The OI values are relatively even and low with values between 25-42 mgCO₂/gTOC for most of the

445

section. The main exception is elevated interval with OI values between 51-94 mgCO₂/gTOC starting at the base of the glauconitic silt (OI rise from 37 to 78 mgCO₂/gTOC at -24.58 m depth) and lasting during the PETM onset up to about -24.32 m depth. The HI/OI ratios is consistently >2 with the exception of the same interval covering the glauconitic silt and the PETM onset between -24.58 to -24.32 m depth where values vary between 0.74-1.33.

450 Both the Terrigenous Aquatic Ratio (TAR) and TOC data is taken from Stokke et al. (2020a). TAR is defined as the ratio of the primarily land-plant derived long-chain *n*-alkanes, over the short-chain *n*-alkanes mainly derived from marine algae (Peters et al., 2005). There is a considerable peak in TAR ~5 cm below Ash SK1, within the glauconitic silt. A second increase in TAR values shortly after the PETM onset (about -24.2 m depth) is followed by gradually decreasing TAR values during the PETM body and recovery. The TOC data shows a pronounced
455 increase from ~0.45 to ~1.3 wt% TOC about 2 cm above the PETM CIE onset (Fig. 9). TOC concentrations remain relatively stable for the lower CIE body, before increasing again in the upper CIE body (from about -13 m depth) up to a maximum of 3.9 wt% at -0.78 m depth (Fig. 10). At the start of the CIE recovery, TOC drops down again to around 1 wt%.

4.54 Major and trace elements of single samples

460 4.4.1 Detrital input

The CIA in the pre-PETM sediments is generally at around 6775, but has one peak of 805 just before the pre-PETM cooling event (-24.64 m depth; Fig. 9) ~~indicating a relative rise in the influx of terrestrially weathered material~~. Following the onset, the CIA ~~rises~~ increases to a maximum of about 7983 at -20.60 m depth, before returning to pre-PETM values in the upper PETM body (Fig. 10). The recovery phase shows increasing CIA values again towards Ash -19, with 8456 at +5.50 m depth.

465 The sediments thermal immaturity was verified by the low RockEval T_{max} values of <422 °C (Table 3, Supplement 1). The HI peaks up to 150 mgHC/gC in the glauconitic silt between -24.61 to -24.59 m depth, but is otherwise <100 mgHC/gC pre-PETM (Fig. 9). The HI increases >100 mgHC/gC about 13 cm above the CIE onset at -24.05 m depth. A second major increase in HI occurs above -14 m depth, after which values remain high and reaches
470 maximum values of 303 mgHC/gC at -0.78 m depth (Fig. 10).

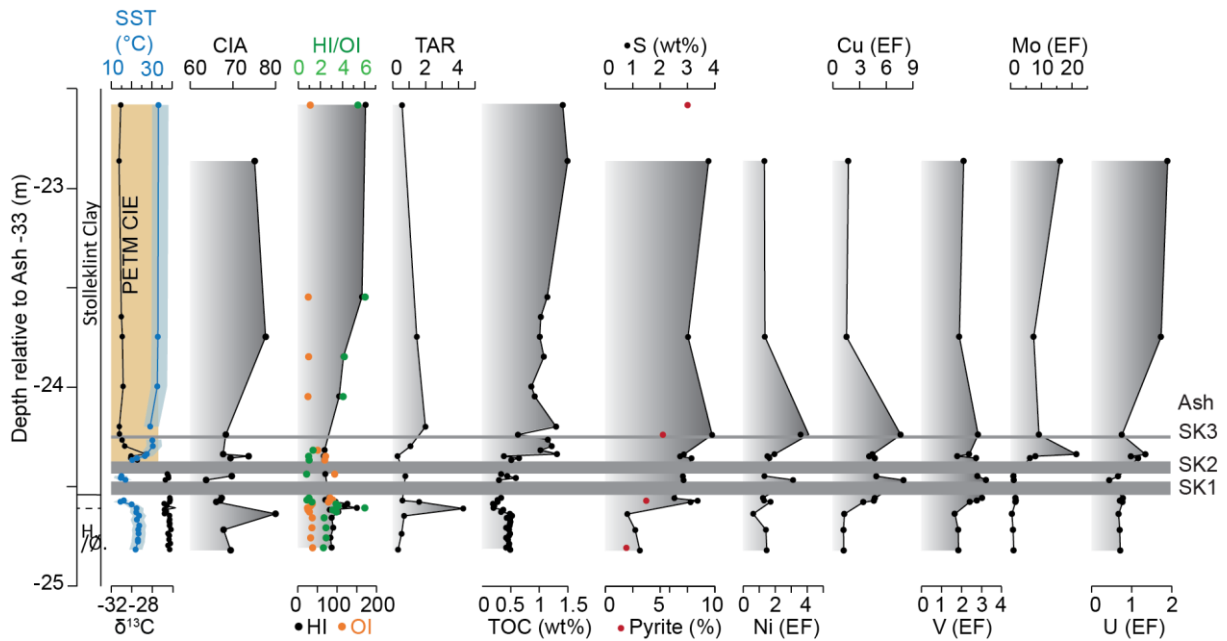


Figure 9: The lowermost 2.5 m of the Stolleklint beach section showing a close-up of the CIE onset. Graphs show: TEX₈₆ data from Stokke et al. (2020a); $\delta^{13}\text{C}$ and Total Organic Carbon (TOC) data from Jones et al. (2019); Chemical Index of Alteration (CIA); Hydrogen Index (HI) and Oxygen Index (OI) where vertical line divide between dominantly terrigenous (<100) and marine (>100) organic material; Terrigenous Aquatic Ratio (TAR) from Stokke et al. (2020a); fraction of pyrite from bulk XRD analyses; S concentrations in wt%; trace metal enrichment factors of Ni, Cu, U, Mo, and V. productivity proxies Ni, Cu, P_2O_5 , and Ba normalised to Al_2O_3 ; fraction of pyrite from bulk XRD analyses; S concentrations in wt%; Th/U ratio where vertical line divide anoxic (<2) from oxic (2-7) sediments; molybdenum concentrations in ppm where vertical line divide between anoxic (<30 ppm) and euxinic (>30 ppm); V normalised to Al_2O_3 .

4.4.2 Productivity

The TOC data shows a pronounced increase from 0.45 to 1.3 wt% TOC about 2 cm above the PETM CIE onset (Fig. 9). TOC concentrations remain relatively stable for the lower CIE body, before increasing again in the upper CIE body (from about 13 m depth) up to a maximum of 3.9 wt% at 0.78 m depth (Fig. 10). At the start of the CIE recovery, TOC drops down again to around 1 wt%.

Both S and pyrite concentrations start to rise before Ash SK1 and the CIE onset, with S increasing from about 1 wt% in the Holmehus/Østerrende Formation to about 3 wt% in the glauconitic silt (Fig. 9). Sulfur concentrations remain high throughout the CIE body, with maximum values of 4.6 wt% reached at -8.6 m depth (Fig. 10). Th/U decreases below Ash SK1 and reaches values below 2 before the CIE onset (Fig. 9). In the lower CIE body between -20.60 to -16.68 m depth Th/U increases up to 3, coinciding with slightly lowered S concentrations (Fig. 10). Th/U values decreases again and persist below 2 for the remaining CIE body (Fig. 10), as U concentrations are enriched up to 11.4 ppm (Table 4, Supplement 1), well above average crustal values of 2.8 ppm (Taylor and McLennan, 1995).

While Cu_{EF} and V_{EF} have values consistently >1 indicating a constant relative enrichment, Ni_{EF} show overall lower EF values and some depletion with 5 samples <1. Before the CIE onset $\text{Ba}/\text{Al}_2\text{O}_3$ decreases from the base of the glauconitic silt, while $\text{Cu}/\text{Al}_2\text{O}_3$ increases, and $\text{Ni}/\text{Al}_2\text{O}_3$ and $\text{P}_2\text{O}_5/\text{Al}_2\text{O}_3$ remain relatively stable (Fig. 9). Before the CIE onset Cu_{EF} and V_{EF} values rises from the base of the glauconitic silt (at -24.58 m depth), while Ni_{EF} remain

relatively stable (Fig. 9). Vanadium, Both Cu and Ni are elements typically associated with volcanic ash, and both remain they all show a relative enrichmently-high within the lower ash-rich interval, with particularly Cu and Ni peaking around ash layers SK1 and SK3. All three elements decrease to lower values in the lower PETM body, before increasing in the upper half (Fig. 10). However, while Cu_{EF} and V_{EF} continue to increase until the recovery, Ni_{EF} decreases slightly about 5 m below Ash -33. The main increase in productivity proxies occurs within the uppermost CIE body between about -8.56 m depth and Ash -33 (Fig. 10). This trend is most notable in Ba/Al_2O_3 and P_2O_5/Al_2O_3 , reaching maximum values of 49.8 and 0.017 respectively at -4.48 m depth. Cu/Al_2O_3 shows a similar although less distinct trend with the main increase in the upper CIE body, while Ni/Al_2O_3 decreases much earlier at about -5 m depth. During the recovery Ba/Al_2O_3 and P_2O_5/Al_2O_3 decreases, while Cu/Al_2O_3 and Ni/Al_2O_3 remain relatively stable (Fig. 10).

Uranium appears to be depleted below the PETM onset with U_{EF} values consistently <1 and particularly low values above ash layers SK1 and SK3 (Fig. 9). Immediately above the CIE onset U_{EF} rises >1 (at -24.36 m depth), although it does not become consistently enriched until about -23.75 m depth. Molybdenum is also depleted in the lowermost part of the section, with Mo_{EF} rising >1 at the base of the glauconitic silt (-24.8 m depth; Fig. 9). However, Mo_{EF} still does not increase substantially until after the CIE onset (at -24.36 m depth) similar to U_{EF} . Both U_{EF} and Mo_{EF} remain relatively stable around 1.3 and 10 respectively in the lower part of the PETM body, but increases dramatically in the upper, non-laminated part before decreasing again during the recovery (Fig. 10). While U_{EF} reaches maximum values of about 5.2 (at -1.34 m depth), Mo_{EF} increases substantially with values of about 30-38 between -8.56 to -0.11 m depth (Fig. 10; Supplement).

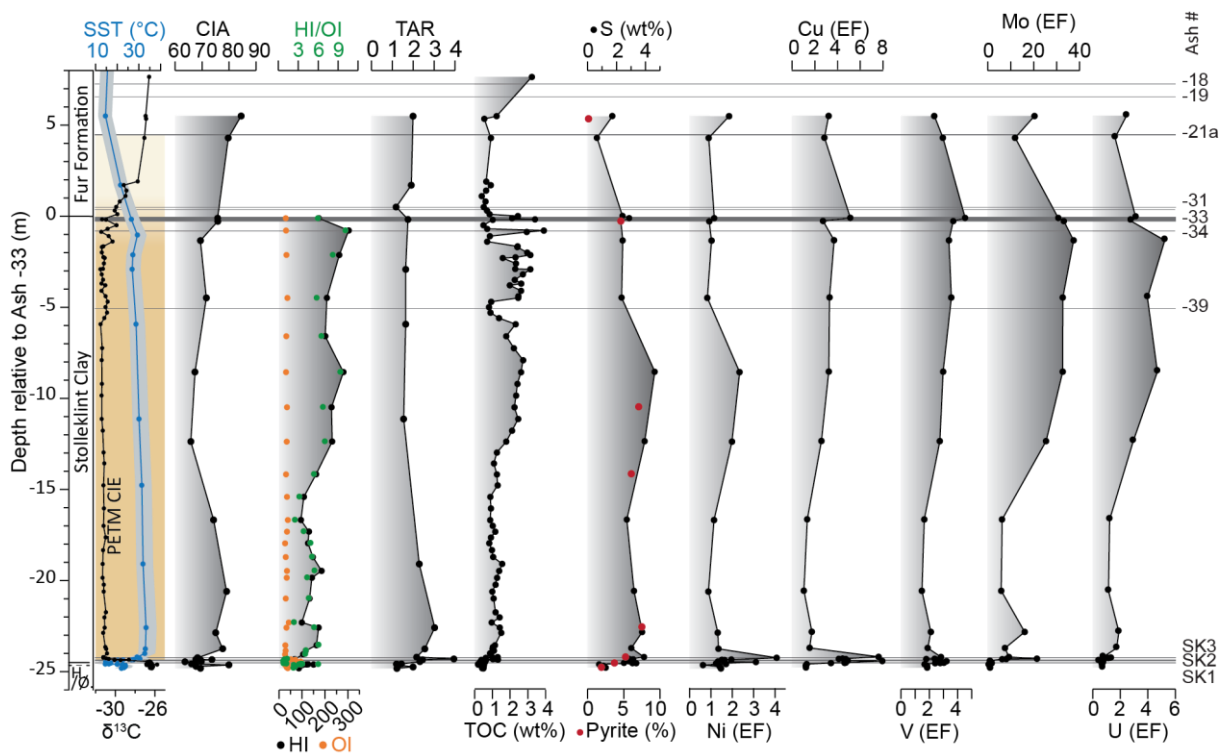


Figure 10: The section covering the whole Stolleklint PETM, with some additional samples from the nearby quarry FQ16 (Fig. 9) between -5.6 and 2 m depth. See Figure 9 for details on each graph.

4.4.3 Redox

Both S and pyrite concentrations start to rise before Ash SK1 and the CIE onset, with S increasing from about 1 wt% in the Holmehus/Østerrende Formation to about 3 wt% in the glauconitic silt (Fig. 9). Sulfur concentrations remain high throughout the CIE body, with maximum values of 4.6 wt% reached at 8.6 m depth (Fig. 10). Th/U decreases below Ash SK1 and reaches values below 2 before the CIE onset (Fig. 9). In the lower CIE body between 20.60 to 16.68 m depth Th/U increases up to 3, coinciding with slightly lowered S concentrations (Fig. 10). Th/U values decrease again and persist below 2 for the remaining CIE body (Fig. 10), as U concentrations are enriched up to 11.4 ppm (Table 4, Supplement 1), well above average crustal values of 2.8 ppm (Taylor and McLennan, 1995).

Molybdenum concentrations vary between 0.7–3.0 ppm below the CIE onset, before increasing to ~15 ppm about 2 cm above the CIE onset (Fig. 9). Molybdenum concentrations continue between 11–43 ppm indicating anoxic conditions prevail throughout the CIE body and recovery, with euxinic conditions (>30 ppm Mo) indicated in the upper CIE body between 12.4 to 0.1 m depth (Fig. 10).

V/Al₂O₃ increases in the glauconitic silt and remain relatively high in the ash interval (Fig. 9). Vanadium enrichments can also be associated with ash deposition, which might affect V concentrations in this particularly ash rich interval. V/Al₂O₃ values increase gradually throughout the CIE body, reaching maximum just below Ash 33 at 0.11 m depth, and decreases again in the recovery (Fig. 10).

5. Discussion

5.1 Changing sediment input – tectonic and climatic influence

5.1.1 Illite–Smectite—importance and origin

Smectite is the dominant clay mineral within the pre-PETM and most of the earliest Eocene strata at both Fur (Fig. 4) and generally in the North Sea (Nielsen et al., 2015). Clay mineral assemblages have been used as indicators of palaeoclimate, most commonly using kaolinite as a proxy for humid tropical climates and smectite for warm climates with seasonal humidity and longer dry spells (e.g. Thiry, 2000). However, soil formation is a slow process, and the subsequent long duration between formation and deposition in a marine basin suggests that clay mineralogy is an unreliable palaeoclimate proxy at resolutions shorter than 1 Myr (Thiry, 2000). Changes in the clay mineral assemblage in the marine sediments may therefore instead indicate changes in source area and intensity of sediment transport, and reflect the climatic conditions at the time of continental soil formation rather than at the time of deposition (Thiry, 2000; Nielsen et al., 2015). Smectite is a common weathering product of mafic volcanic material (Stefánsson and Gíslason, 2001), and previous studies have suggested that smectites in the Danish stratigraphic record are of predominantly volcanic origin (Nielsen and Heilmann Clausen, 1988; Pedersen et al., 2004). Although smectite may precipitate *in situ* from hydrothermal fluids, this has largely been discounted in the North Sea due to the wide geographic extent of smectite and the overall lack of indices of hydrothermal influence (Huggett and Knox, 2006; Kemp et al., 2016). *In situ* post-depositional alteration of volcanic ash also probably contributed only minor amounts of smectite, as the ashes are mostly relatively well preserved (Nilsen et al., 2015). While clay minerals make up a small fraction of the bulk mineralogy in the upper PETM body (4–8%), zeolites

555 comprise up to 36 % (Fig. 4). Zeolites are another typical weathering product of volcanic materials, supporting a volcanic provenance (Stefánsson and Gíslason, 2001; Nielsen et al., 2015).

The volcanic source is likely to be the NAIP. Major flood basalts erupted in East Greenland, the Faroe Islands, and the British Isles across the Paleocene–Eocene boundary, producing large uplifted areas several km high of easily eroded material (Larsen and Tegner, 2006; Storey et al., 2007b; Wilkinson et al., 2017). This is reflected in Os isotopes and CIA records in the Arctic Ocean, which record an influx of weathered volcanic material both prior to and during the PETM (Wieczorek et al., 2013; Dickson et al., 2015). Moreover, the first phase of ash deposition was identified within Late Paleocene strata in the North Sea, well before the PETM onset (Knox and Morton, 1988; Haaland et al., 2000). Erosion and redeposition of altered tephra deposited around the North Sea likely constituted a highly important source for the volcanic material in the North Sea basins (Pedersen et al., 2004; Nielsen et al., 2015; Kemp et al., 2016). Smectite is found in abundance throughout the North Sea stratigraphic record, and decreases as ash deposition ceases upward in the Eocene (Nielsen et al., 2015; Kemp et al., 2016). It seems likely that the dominance of smectite and abundance of zeolites reflect this extensive extrusive volcanism around the NAIP (Nielsen et al., 2015; Kemp et al., 2016).

5.1.12 Kaolinite and changes in weathering across the PETM onset

570 At Fur, there is a substantial influx of kaolinite in the lowermost 10 m of the PETM CIE (Fig. 4). The pulse of kaolinite initiates shortly after the CIE onset and again in the CIE recovery, in both instances concordant with a rise in the CIA and in the bulk mineralogy clay fraction (Figs. 4, 10). As the clay fraction in the strata above and below the kaolinite pulse is dominated by smectite, it suggests some major change in climate and/or sediment supply occurs within the lower part of the PETM stratigraphy. Clay mineral assemblages have been used as
575 indicators of palaeoclimate, most commonly using kaolinite as a proxy for humid tropical climates and smectite for warm climates with seasonal humidity and longer dry spells (Bolle et al., 2000; Thiry, 2000). However, soil formation is a slow process, and the subsequent long duration between formation and deposition in a marine basin suggests that clay mineralogy is an unreliable palaeoclimate proxy at resolutions shorter than 1 Myr (Thiry, 2000). Changes in the clay mineral assemblage in the marine sediments is therefore unlikely to reflect an increase in
580 continental soil production induced by changing temperatures and humidity (Carmichael et al., 2017).

An increase in kaolinite content during the PETM is observed globally (Robert and Kennett, 1994; Dypvik et al., 2011; John et al., 2012; Khozyem et al., 2013; Bornemann et al., 2014; Kemp et al., 2016), yet the timing and magnitude varies considerably even within the North Sea (Kender et al., 2012; Kemp et al., 2016). In the western North Sea, the kaolinite content increase earlier before and during the CIE onset and again during the CIE recovery, but is relatively low in the CIE body (Kender et al., 2012; Kemp et al., 2016). However, at Fur a rise in the kaolinite content is not observed until after the CIE onset (Fig. 4), and southward in the Bay of Biscay in the North Atlantic the kaolinite content does not significantly change until the PETM recovery (Bornemann et al., 2014). It would be expected that changes in the climate and the hydrological cycle would be broadly similar within such a narrow region. It is therefore reasonable to assume that the timing and extent of kaolinite deposition depends just as much
590 on the availability and proximity to potential source areas as the climatic conditions. Kender et al. (2012) suggested that the initiation of the kaolinite pulse before the CIE in the central North Sea was due to the thermal uplift and short-lived regression in the latest Paleocene. A drop in sea level exposes larger areas to erosion and brings river mouths closer to the marginal marine areas, which could subsequently trigger an influx of terrestrially derived

material. A peak in the HI, TAR and CIA just below the glauconitic silt suggest that a similar short-lived regression is recorded also in Denmark (Fig. 9). However, as the kaolinite pulse at Fur occurs after the CIE and major temperature increase (Fig. 10), it substantially post-dates sea level fall and major tectonic uplift in the latest Paleocene. This suggest that some other trigger than sea-level fall activated the shift to kaolinite deposition in Denmark.

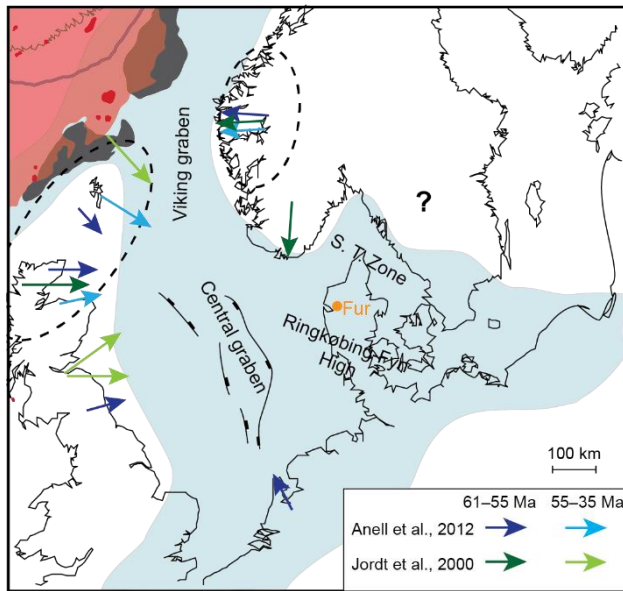


Figure 11: Close up of Figure 1 with modifications based on Schiøler et al. (2007). See Figure 1a for colour legend. Dashed circles indicate main sedimentary source areas for the North Sea during the Paleocene and Eocene from Anell et al. (2012). Arrows indicate the main sediment transport directions based on Jordt et al. (2000) and Anell et al. (2012).

Kaolinite particles are relatively large and heavy and typically deposited closer to the source than finer clays like smectite (Gibbs, 1977; Nielsen et al., 2015). Nielsen et al. (2015) found that deposition of kaolinite in the Paleocene–Eocene North Sea thickens substantially towards the Fennoscandian shield, and suggest that this as the main source area for the Danish sediments. The Fennoscandian shield was characterised by deeply weathered bedrocks in the Paleogene, reflecting the warm tropical Mesozoic climate (Nielsen et al., 2015), and would therefore be enriched in kaolinite. Considering the typically shorter transport of kaolinite (Gibbs, 1977) and the Danish areas distal position in relation to the NAIP (Figs. 1, 11) it seems likely that the main source of kaolinite was from the Fennoscandian Shield to the north and northeast, despite the main sediment source for the North Sea as a whole during this period being from the west and northwest (Fig. 11; Jordt et al., 2000; Anell et al., 2012). A North Sea surface water freshening is suggested from palynology and shark-tooth apatite $\delta^{18}\text{O}$ values in the central North Sea (Zacke et al., 2009; Kender et al., 2012). The global influx in kaolinite has generally been attributed to an intensified hydrological cycle leading to enhanced erosion and sediment transport of older deeply weathered bedrock and soils (Schmitz and Pujalte, 2003; John et al., 2012; Bornemann et al., 2014; Carmichael et al., 2017). It therefore seems likely that the observed influx of kaolinite, increased CIA, and rapid intensification of sedimentation rates after the CIE onset at Fur is the result of increased erosion and runoff from the deeply weathered Fennoscandian bedrock. Considering the potential time-lag between increased runoff and final marine deposition, this indicates a rapid response in the hydrological cycle to changes in temperature and carbon emissions across the PETM onset.

625 An important deviation from the smectite dominance is the substantial influx of kaolinite in the lowermost 10 m of the PETM CIE (Fig. 4). The abundance of kaolinite at Fur grows rises shortly after the CIE onset and again in the CIE recovery, in both instances concordant with a risen increase in the CIA and the overall clay fraction (Figs. 4, 10). An increase in kaolinite content during the PETM is observed globally (Robert and Kennett, 1994; Dypvik et al., 2011; John et al., 2012; Khozyem et al., 2013; Bornemann et al., 2014; Kemp et al., 2016). While it was initially attributed to a warmer and more humid climate (e.g. Bolle et al., 2000), it is now generally acknowledged that the formation of kaolinite requires too much time (1–2 Myr; Thiry, 2000) to be a direct result of climate on such short timescales (Carmichael et al., 2017). The increase in kaolinite is therefore most likely due to an intensified hydrological cycle, leading to enhanced erosion and sediment transport of older deeply weathered bedrock and soils (Schmitz and Pujalte, 2003; John et al., 2012; Bornemann et al., 2014).

630 Although the kaolinite pulse appears to be global, the timing and magnitude varies a great deal considerably even within the North Sea (Kender et al., 2012; Kemp et al., 2016). In the western North Sea, the kaolinite content increases earlier before and during the CIE onset and again similarly during the CIE recovery, but is relatively low in the CIE body (Kender et al., 2012; Kemp et al., 2016). However, at Fur a kaolinite content increase is not observed until after the CIE onset (Fig. 4), and southward in the Bay of Biscay in the North Atlantic the kaolinite content does not rise at all until the PETM recovery (Bornemann et al., 2014). It would be expected that changes in the climate and the hydrological cycle would be broadly similar within such a narrow region. It is therefore reasonable to assume that the timing and extent of kaolinite deposition depends just as much on the availability and proximity to potential source areas as the climatic conditions.

640 **Figure 11:** Close up of Figure 1 with modifications based on Schiøler et al. (2007). See Figure 1a for colour legend. Dashed circles indicate main sedimentary source areas for the North Sea during the Paleocene and Eocene from Anell et al. (2012). Arrows indicate the main sediment transport directions based on Jordt et al. (2000) and Anell et al. (2012).

645 During the Paleocene and Early Eocene, the major sediment transport direction in the North Sea were from the west and northwest due to the thermal uplift of source areas around the NAIP such as the Faroe–Shetland platform (Fig. 11; Knox, 1996; Anell et al., 2012). Kender et al. (2012) subsequently suggested that the initiation of the kaolinite pulse before the CIE in the central North Sea was due to the thermal uplift and short lived regression in the latest Paleocene. At Fur, there is no pre-PETM pulse of kaolinite and the HI index is >100 within the glauconitic silt (Fig. 9), indicating an increase in aquatic organic matter deposition. However, but there is a peak in the CIA it seems there is also an augmented CIA just below the glauconitic silt (~28 cm below the CIE onset at 24.64 m depth; Fig. 9) and in TAR (24.61 to 24.58 m depth) at and below the base of the glauconitic silt. This, which suggests some increase in the fluxes of terrestrially derived material changes in sediment transport or sea level likely could have occurred also prior to the CIE onset at Fur (Fig. 9). Conversely, the HI also peaks below the base of the glauconitic silt (24.61 m depth) indicating a slight shift to more marine organic matter. Together, this suggests that there may be significant uncertainty regarding the data at and immediately below the glauconitic silt. If the peaks in CIA and TAR are disregarded, there is little evidence of any change in sediment distribution prior to the PETM onset. Stokke et al. (2020a) similarly observed a peak in terrestrially derived long chain *n* alkanes and in soil derived branched GDGTs (*br*GDGTs) around the base of the glauconitic silt, which could reflect a tectonically forced regression due to the NAIP thermal uplift. Kaolinite particles are relatively large and heavy and

660 typically deposited closer to the source than finer clays like smectite (Gibbs, 1977; Nilsen et al., 2015). The reduced response in kaolinite deposition to thermal uplift of the NAIP this tectonic event in Denmark compared to the Central North Sea therefore seems reasonable considering comparably distal position to the NAIP (Figs. 1, 11).

665 The influx of kaolinite at Fur correlates with a major increase in the CIA and starts minimum 12 cm above the CIE onset, and up to 22 cm (excluding Ash SK2) above the Stolleklint Clay base (Figs. 4, 10) — If we assume the boundary base of the Stolleklint Clay is placed at Ash SK1. Changes in mineralogy and the CIA typically reflect some change in the pattern of sediment distribution that can be triggered by many different factors. Nielsen et al. (2015) found that deposition of kaolinite in the Paleocene–Eocene North Sea thickens substantially towards the Fennoscandian shield, and suggest that this as the main source area for the Danish sediments. The Fennoscandian shield was characterised by deeply weathered bedrocks in the Paleogene, reflecting the warm tropical Mesozoic climate (Nielsen et al., 2015), and would therefore be enriched in kaolinite. Considering again the typically shorter transport of kaolinite (Gibbs, 1977) and the Danish areas distal position in relation to the NAIP (Figs. 1, 11) it seems likely that the main source of kaolinite was from the Fennoscandian Shield to the north and northeast, despite the main sediment source for the North Sea during this period being from the west and northwest (Fig. 11; Jordt et al., 2000; Anell et al., 2012). A drop in sea level exposes larger areas to erosion and brings river mouths closer to the marginal marine areas, subsequently triggering an influx of terrestrially derived material that could explain the early Eocene kaolinite and CIA increase in the Danish area. However, the increase post-dates sea level fall and major tectonic uplift in the latest Paleocene, and occurs after the CIE and major temperature increase (Fig. 10). It therefore seems reasonable that it at least partially reflects an intensified hydrological cycle due to climatic changes rather than purely tectonic forcing. Furthermore, a North Sea surface water freshening is suggested from palynology and shark tooth apatite $\delta^{18}\text{O}$ values in the central North Sea (Zacke et al., 2009; Kender et al., 2012). The observed influx of kaolinite, increased CIA, and rapid intensification of sedimentation rates after the CIE onset at Fur are therefore likely to be the result of increased runoff due to an enhanced hydrological cycle.

675 5.1.2 Illite–Smectite – importance and origin

685 Smectite is the dominant clay mineral within the pre-PETM and most of the earliest Eocene strata at both Fur (Fig. 4) and generally in the North Sea (Nielsen et al., 2015). Smectite is a common weathering product of mafic volcanic material (Stefánsson and Gíslason, 2001), and previous studies have suggested that smectites in the Danish stratigraphic record are of predominantly volcanic origin (Nielsen and Heilmann-Clausen, 1988; Pedersen et al., 2004). Although smectite may precipitate *in situ* from hydrothermal fluids, this has largely been discounted in the North Sea due to the wide geographic extent of smectite and the overall lack of indices of hydrothermal influence (Huggett and Knox, 2006; Kemp et al., 2016). *In situ* post-depositional alteration of volcanic ash also probably contributed only minor amounts of smectite, as the ashes are mostly well-preserved (Nilsen et al., 2015). While clay minerals only make up a trace fraction of the bulk mineralogy in the upper PETM body (4–8 %), zeolites comprise up to 36 % (Fig. 4). Zeolites are another typical weathering product of volcanic materials (Stefánsson and Gíslason, 2001; Nielsen et al., 2015), supporting a volcanic provenance.

695 Major flood basalts were emplaced in East Greenland and the Faroe Islands between 56.0 and 55.6 Ma, producing large uplifted areas several km high of easily eroded material (Larsen and Tegner, 2006; Storey et al., 2007b; Wilkinson et al., 2017). This is reflected in Os isotopes and CIA records in the Arctic Ocean, which record an influx of weathered volcanic material both prior to and during the PETM (Wieczorek et al., 2013; Dickson et al.,

2015). Moreover, the first phase of ash deposition was identified within Late Paleocene strata in the North Sea, well before the PETM onset (Knox and Morton, 1988; Haaland et al., 2000). Erosion and redeposition of altered tephra deposited around the North Sea likely constituted a highly important source for the volcanic material in the North Sea basins (Pedersen et al., 2004; Nielsen et al., 2015; Kemp et al., 2016). Smectite is found in abundance throughout the North Sea stratigraphic record, and decreases as ash deposition ceases upward in the Eocene (Nielsen et al., 2015; Kemp et al., 2016). It seems likely that the dominance of smectite and abundance of zeolites reflect this extensive extrusive volcanism around the NAIP (Nielsen et al., 2015; Kemp et al., 2016), highlighting the importance of the NAIP in augmenting silicate weathering during the PETM.

5.2 Volcanic indices

Although the principal component analysis indicate that the glauconitic silt is most like the Holmehus/Østerrende Formation (Fig. 7), the gradual increase in Ti relative to Fe and K shown by the XRF element core scans suggest a gradual change in lithology towards Ash SK1 (Fig. 5). ~~Variations in the major elements Fe, Ti, and K in marine sediments typically indicate changes in the terrigenous fraction (Rothwell and Croudace, 2015).~~ Titanium is generally considered a stable element directly reflecting the coarse-grained terrigenous fraction (Rothwell and Croudace, 2015), but the highly Ti-rich nature of the ashes SK1-4 renders Ti an unreliable proxy for terrigenous input in this particular section and the gradual increase could therefore reflect an influx of terrestrially derived material within the glauconitic silt. This is supported by a slightly coarser grain size, and peaks in the augmented CIA and TAR (Fig. 9), and an influx of terrestrially derived organic matter (Stokke et al., 2020a). However, this influx seems to see that these peaks decline prior to Ash SK1 in contrast to the increase in Ti, and that there is as discussed significant doubt about these peaks, some other cause need to be considered. Titanium can also be used to indicate volcanic provenance, where K and Ti reflect felsic and mafic sources respectively (Rothwell and Croudace, 2015). In fact, the K/Ti ratio has been applied as a useful proxy for felsic/mafic provenance in the North Atlantic (Richter et al., 2006). ~~The SK ashes are all highly titanium rich (Figs. 5), and it could indicate be that we see~~ a gradual rise in mafic volcanic activity before the main ash deposition (Fig 5). ~~This is corroborated by the~~ Estimates of the timing and duration of the East Greenland lava eruptions, ~~which suggests~~ that a 5–6 km thick lava pile was emplaced between 56.0 and 55.6 Ma (Larsen and Tegner, 2006), ~~indicating that there was voluminous mafic NAIP activity during this period.~~ The trace metals Cu, Ni, and V are also found to increase within the glauconitic silt (Fig. 9), all of which are typically associated with volcanic material and maintain high concentrations within the SK1–SK2 interval.

An amplified influx of weathered basaltic material such as smectite could also cause the gradually increased Ti flux. However, smectite is already the dominant clay phase in the Holmehus/Østerrende Formation (Fig. 4), and does not show a significant rise in the glauconitic ~~silt~~ clay. It therefore seems that the augmented Ti concentrations within the glauconitic silt might be caused by an increased ash component, rather than from basaltic weathering. ~~The trace metals Cu, Ni, and V are also found to increase within the glauconitic silt (Fig. 9), all of which are typically associated with volcanic material and maintain high concentrations within the SK1–SK2 interval.~~ Such volcanic ash deposits that are not visible to the naked eye are called cryptotephra, and typically include glass shards and crystals together with non-volcanic deposits (Cassidy et al., 2014). It is possible that the glauconitic silt includes an increasing portion of cryptotephra prior to the large eruptions producing ashes SK1 and SK2. ~~In our A~~ previous study, ~~we~~ found that SSTs cooled prior to the PETM onset in Denmark (Stokke et al., 2020a). Although

the cooling started within the glauconitic silt below Ash SK1 (Fig. 9), ~~they~~we proposed that it could be a result of volcanic cooling induced by SO₂ aerosols from NAIP eruptions (Stokke et al., 2020a). The observation of a potentially increasing ash component already within this glauconitic unit could be supportive of a ~~potentially~~ volcanically induced cooling.

The identified tephra layers in Denmark represent explosive eruptions with an unusually large magnitude in order to be transported such a long distance (Stokke et al., 2020b). The absence of visible tephra layers therefore does not automatically mean that there was no tephra producing eruptions during the PETM. Besides two thin ash layers about 10 and 12 cm above Ash SK2, there are no visible ash layers during the PETM body until the deposition of Ash -39 at about -5 m depth (Fig. 4). However, the box cores allow for a detailed and high resolution overview that might reveal the presence of ash rich intervals earlier. Figure 6 section D shows correlating changes in S, Ca, Fe/Ti, Fe/K, and K/Ti between about -10.81 to -10.48 m depth. The presence of cryptotephra layers is particularly likely when low K/Ti ratios correlate with increases in Fe/Ti and Ca, and to some extent S. Relative changes in Fe/Ti – and to some extent Ca – depend strongly on the source of the volcanic material. These results indicate four possible ash rich horizons within the dark clays, which could be cryptotephra of slightly variable chemistry (Fig. 6 section D). This suggests that explosive volcanic eruptions at a scale substantial enough for some material to reach Denmark may also have occurred during the PETM body. However, much more detailed work is needed in order to confirm the presence or absence of tephra fall deposits during this interval.

5.3 Changes in basin oxygenationicity

~~5.3.1 Oxidation–anoxic shift across the PETM onset~~

The ~~PETM CIE is concordant with a~~ lithological shift from the bioturbated Holmehus/Østerrende Formation to the laminated Stolleklint Clay, reflecting a ~~shift to a suboxic to anoxic~~ change in the oxygen content in the bottom water environment. An increase in S, pyrite, ~~and V_{EF}/Al, and U (seen as a decrease in Th/U)~~ within the glauconitic silt could indicate reducing conditions had already initiated below the laminations, prior to the CIE onset (Fig. 9). ~~The NAIP uplift led to the closing of ocean seaways and North Sea Basin restriction prior to the CIE, resulting in increased halocline stratification that could explain this early deoxygenation (Kender et al., 2012).~~ However, this is contrary to the low organic content, abundant bioturbation, and high content of glauconite, suggesting that an oxygenated environment prevailed pre-PETM. An oxic environment has also been indicated by the relatively high values of the organic biomarker pristane/phytane indicating oxidation of phytol to pristane (Stokke et al., 2020a). Sluijs et al. (2014) explained a similar co-occurrence of oxic and euxinic proxies within a section in the Gulf of Mexico as the result of seasonal to decadal variations in basin oxygenationicity. Alternatively, ~~the increase in S, U, and V_{it}~~ could be attributed to post-depositional authigenic enrichment due to deposition of ash layer SK1 ~~an increased ash component within the glauconitic silt,~~ as volcanic tephra deposits can reduce the sediment pore waters oxygen levels just below an ash layer (Hembury et al., 2012). ~~An increase in the sedimentary ash component has already been suggested based on the high resolution XRF element core scans (Fig. 5), and the increase in ICP-MS analyses of Ni and Cu (Fig. 9).~~ However, the highly redox-sensitive elements Mo and U does not show a similar increase below the CIE. On the contrary, a U_{EF}<1 suggest the sediments are rather depleted in U (Fig. 9). Both the high-resolution XRF element core scans and ICP-MS analyses of Ni and Cu indicate an increased ash component within the sediments just below ash SK1. These contradictory observations could be explained by a

large component of volcanic ash with the sediments, which is expected to have relatively high concentrations of both V and S.

~~The burial rate of Mo increases three orders of magnitude in sulfidic environments relative to oxic, as Mo becomes highly reactive in the presence of hydrogen sulfide (Tribovillard et al., 2004; Scott and Lyons, 2012). Molybdenum enrichment above bulk crustal values (1–2 ppm; Taylor and McLennan, 1995) indicates suboxic to anoxic conditions, and enrichments >30 ppm are argued to indicate euxinic conditions (Scott and Lyons, 2012; Dickson et al., 2014). Molybdenum concentrations at Stolleklint do not increase substantially above 3 ppm until after the CIE, suggesting that a substantial decrease in oxicity does not occur until after the PETM onset.~~

Laminations occur ~~rapidly only 2 cm above~~ after the CIE onset, together with an increase in S and Fe/Ti in XRF element core scans (Fig. 5 section B). Iron and Ti in marine sediments commonly co-vary, and elevated Fe/Ti ratios therefore indicate excess Fe over basaltic lithogenic values (Marsh et al., 2007). Fe is redox-sensitive and may also reflect changes in basin oxygenation post-deposition (Rothwell and Croudace, 2015). An increase of Fe relative to Ti or K may therefore indicate suboxic conditions, particularly in concert with increased S content (e.g. Sluijs et al., 2009). TOC_c and Mo_{EF} and U_{EF} concentrations, as well as continued low Th/U values (Fig. 10) also rises substantially at the base of the laminations, with Mo_{EF} rising above 6. The burial rate of Mo increases three orders of magnitude in sulfidic environments relative to oxic, as Mo becomes highly reactive in the presence of hydrogen sulfide (Tribovillard et al., 2004; Scott and Lyons, 2012). And, although the values are somewhat tentative, Mo_{EF} and U_{EF} values between about 3-10 have been related to suboxic conditions (Algeo and Tribovillard, 2009; Tribovillard et al., 2012). In addition A previous study from the exact same section at Stolleklint also found that photic zone euxinia may have occurred just after the CIE onset, as indicated by the presence of sulfur bound isorenieratane; a diagenetic product of green sulfur bacteria (Schoon et al., 2015).

~~The XRF element core scans also show an increase in S and Fe/Ti at base of the laminated sediments (Fig. 5 section B). Iron and Ti in marine sediments commonly co-vary, and elevated Fe/Ti ratios therefore indicate excess Fe over basaltic lithogenic values (Marsh et al., 2007). While Ti is considered a stable element that directly reflects the coarse grained terrigenous fraction, Fe is redox sensitive and may also reflect changes in basin oxygenation post deposition (Rothwell and Croudace, 2015). An increase of Fe relative to Ti or K may therefore indicate suboxic conditions, particularly in concert with increased S content (e.g. Sluijs et al., 2009). We therefore conclude that while there may be some uncertainty as to when oxic conditions started to deteriorate due to the high content of ash, the start of laminations about 2 cm above Ash SK2 and the CIE onset indicate the initiation of at least periodically fully anoxic conditions at Stolleklint. In addition, the XRF element core scans document a direct correlation between elevated S and Fe/Ti, and the dark laminations (Fig. 6 section C), suggesting regular fluctuations in basin deoxygenation in the lower part of the PETM body.~~

In the upper part of the PETM body the Stolleklint Clay becomes apparently structureless and almost black. Here XRF S counts show continuous high values (Fig. 8), suggesting that reducing conditions become more or less continuous. The TOC content and the trace metals Cu_{EF}, V_{EF}, and particularly Mo_{EF}, and U_{EF} increases similarly in the dark upper half with Mo_{EF} up to ~37 and U_{EF} up to ~5 (Fig. 10). Pyrite, S (wt%), and Ni_{EF} values show a similar increase initially, but decreases above ash -39 (Fig. 10). Mo_{EF}>10 may indicate euxinic conditions (Algeo and Tribovillard, 2009; Tribovillard et al., 2012), although the comparatively lower enrichment of U may also suggest that some other factor is enhancing Mo enrichment in the sediments such as the “particle shuttle” effect

815 (Algeo and Tribovillard, 2009) or enhanced Mo-trapping by sulfurized marine organic matter (Tribovillard et al.,
2004; Algeo and Tribovillard, 2020). Schoon et al. (2015) argued that photic zone euxinia prevailed during the
entire PETM interval both at Stolleklint and Store Bælt (Fig. 1) based on the presence of green sulfur bacteria.
Unfortunately, their data from Stolleklint only covers the lowermost 2.5 m and uppermost 0.5 m of the Stolleklint
Clay, and therefore excludes most of the PETM body. It therefore seems there is little independent evidence in
820 support of a euxinic environment prevailing throughout the PETM. We therefore conclude that the PETM in
Denmark was characterised by an anoxic to sulfidic environment that become increasingly prevalent during the
PETM body.

5.3.2 Redox and productivity changes during the PETM body

825 Schoon et al. (2015) argued that photic zone euxinia prevailed during the entire PETM interval in two sedimentary
sections in Denmark. Unfortunately, their data from Fur only covers the lowermost 2.5 m and uppermost 0.5 m of
the Stolleklint Clay, and therefore excludes most of the PETM body. All proxies from our continuous record
through the PETM body suggest that anoxia prevailed throughout (Fig. 9), but the proxies also indicate distinct
stratigraphic variations in basin oxicity. The XRF element core scans document a direct correlation between
elevated S and Fe/Ti, and the dark laminations (Fig. 6 section C), suggesting regular fluctuations in basin oxicity
830 (approximately every 2 cm). Variations in basin anoxia is also indicated for longer periods. The biplot of S data
from XRF element core scans (Fig. 8) indicate an overall stratigraphic upward increase in basin anoxia. The upward
decrease in scatter in the S measurements also indicates that anoxic conditions becomes gradually more continuous
with time (Fig. 8).

835 While Th is sourced from continental weathering and unreactive to redox changes, U has minimal detrital influence
and is enriched in the sediments under reducing conditions (Tribovillard et al., 2006). The Th/U ratio therefore
reflects U enrichment above crustal values, and can be employed to assess basin oxicity (Wignall and Myers, 1988;
Dypvik et al., 2011; Elrick et al., 2017). Th/U is about 4 in the average upper crust, and typically <2 in anoxic
environments with substantial authigenic U enrichment (Wignall and Twitchett, 1996). An increase in Th/U above
2 correlates with a decrease in Mo concentrations well below 30 ppm around 17 to 18 m depth in the lower
840 laminated part, indicating a period of less anoxic conditions in the lower PETM body (Fig. 10). Both U and Mo
concentrations increase substantially in the upper PETM body, with Th/U <2 and Mo well above 30 ppm indicating
euxinic conditions (Fig. 10). Maximum values of S, pyrite and V/Al within this interval also indicate highly
reducing conditions, with high TOC of 4 wt% indicating augmented burial rate of organic matter.

845 The North Sea Basin became very restricted in the NAIP uplift in the latest Paleocene- led to closing of ocean
seaways and North Sea Basin restriction prior to deposition of ash SK1 prior to initiation of seafloor spreading and
basin subsidence, resulting in poor circulation and halocline stratification that could explain an early
deoxygenation in the basin (Knox et al., 2010; Kender et al., 2012). While this could explain the initial decrease
in basin oxygenation below the SK ashes and the CIE onset, there is no further evidence supporting regional
uplift and North Sea basin restriction following associated with the PETM CIE onset. On the contrary, high HI (Fig.
850 10), and low input of *brGDGTs* and long-chained *n*-alkanes (Stokke et al., 2020a) suggest that marine-derived
organic matter increases up stratigraphy, as the Stolleklint Clay was likely deposited during a relative sea level rise
(Heilmann-Clausen, 1995). Kender et al. (2012) found evidence of low surface water salinity and extensive
stratification in the North Sea, and suggested this as the main cause of anoxia during the PETM. The dark massive

855 clays in the upper part of the PETM body is strongly enriched in organic matter (TOC up to 2.9 wt%) and Cu (Cu_{EF} up to 5.1), which both may indicate an increase in productivity (Tribovillard et al., 2006). A combination of ocean stratification and increased productivity would efficiently contribute to the increase in basin anoxia in the upper PETM body.

860 ~~Barium is closely related to export productivity, as it precipitates from decaying organic matter (Paytan and Griffith, 2007; Ma et al., 2014). The sedimentary Ba content is at its highest during the upper PETM body, as is P₂O₅ (an essential macronutrient), indicating that export productivity was at its highest at this point (Fig. 10; Table 4, Supplement 1). Possible remobilisation of Ba and P needs to be considered, particularly in sulfidic environments (Tribovillard et al., 2006). However, the dark massive clay in the upper PETM body is also highly enriched in organic matter (TOC up to 3.9 wt%). An increase in TOC could reflect declining terrestrial influx, possibly due to the increasing sea level, which is expected to lead to a decrease in terrestrial sediment transport to marginal areas (e.g. Carmichael et al., 2017). Still, the combined elevation of TOC, Ba/Al, and P₂O₅/Al, as well as to some extent Ni/Al and Cu/Al (Fig. 10), are all in support of an increase in export productivity. Kender et al. (2012) found evidence of low surface water salinity and extensive stratification in the North Sea, and suggested this as the main cause of anoxia during the PETM. A combination of ocean stratification and increased productivity would efficiently contribute to the increase in basin anoxia in the upper PETM body.~~

870 **5.4 Carbon drawdown – ~~t~~The PETM recovery**

875 ~~The PETM carbon cycle perturbations are unusual both in magnitude and duration, and likely a result of a combination of triggers and feedback mechanisms that are not yet fully understood (McInerney and Wing, 2011; Komar and Zeebe, 2017). Continuous emissions from a light carbon source such as thermogenic degassing around the NAIP could have contributed to the long duration (Svensen et al., 2004; Frieling et al. 2016). Another suggestion is that an initial pulse of light carbon led to warming (e.g. Frieling et al., 2019), subsequently activating positive feedback mechanisms producing continued input of light carbon emissions from sources such as methane clathrates (Dickens et al. 1995) or terrestrial organic carbon (Bowen 2013). Another key PETM feature is the rapidity of the PETM recovery (e.g. Bowen and Zachos, 2010). The carbon cycle recovery occurs through a combination of natural carbon sequestration and negative feedback mechanisms reducing the atmospheric CO₂ content (McInerney and Wing, 2011). Silicate weathering and denudation is perhaps the most important negative feedback mechanisms driving CO₂ drawdown (Gislason and Oelkers, 2011), and have been proposed as one of the most important drivers during the PETM recovery (Kelly et al., 2005; Torfstein et al., 2010; Penman, 2016).~~

880 ~~Silicate weathering is highly sensitive to runoff, temperature, and topography (Gislason and Oelkers, 2011). Temperatures rose globally both before and during the PETM onset (Frieling et al., 2017; Frieling et al., 2019). At Stolleklint, temperatures rose at least 10 °C immediately after following the onset, with at least 10 °C reaching maximum SSTs of ~33 °C about 0.6 m above the CIE onset (Fig. 9) shortly after the CIE onset, followed by a shift to gradually decreasing SSTs throughout the PETM body and recovery (Fig. 9; Stokke et al., 2020a). Silicate weathering is highly sensitive to runoff, temperature, and topography (Gislason and Oelkers, 2011). The warming combined with the increased runoff, indicated in the North Sea by enhanced surface water freshening (Zacke et al., 2009; Kender et al., 2012), would result in a warm and humid climate ideal for increased silicate weathering and denudation. This is supported by the~~
885 At Stolleklint, we see a rapid response in continental weathering and runoff to changes in carbon cycle and temperature. This is indicated by the large increase in sedimentation rate,
890

895 ~~and the influx of weathered material from the Fennoscandian shield suggested by the rise in kaolinite influx, and the CIA shortly after the PETM onset at Stolleklint (Figs. 4, 10), suggesting a rapid response in weathering to changes in carbon cycle and temperature. Fresh basaltic volcanic terrains are particularly prone to weathering, and constitute one of the main sources of weathered suspended material in the world's oceans (Gislason and Oelkers, 2011).~~ While both the kaolinite content and the CIA decreases in the upper PETM body, the sedimentation rate likely remained high, suggesting a relatively rapid influx of other minerals such as the volcanically derived smectite and zeolite. Fresh basaltic volcanic terrains are particularly prone to weathering, and constitute one of the main
900 sources of weathered suspended material in the world's oceans (Gislason and Oelkers, 2011). The extensive NAIP flood basalt volcanism before and during the PETM (e.g. Larsen and Tegner, 2006) may therefore have played an important role in the enhanced silicate weathering, as reflected in the dominance of smectite within the North Sea (Nilsen et al., 2015). ~~A second increase in both the CIA and the kaolinite content occur during the CIE recovery at Fur (Figs. 4, 10), as well as further west in the North Sea (Kender et al., 2012; Kemp et al., 2016), supporting an important role of enhanced silicate weathering in the PETM recovery.~~

905 ~~We have documented a relatively rapid rise in silicate weathering as a response to carbon emissions, but a major increase in export productivity and organic carbon burial (seen as a rise in TOC) is delayed until the upper PETM body. The augmented organic matter burial (increased TOC) in concert with the high Cu_{EF} (Fig. 10) suggest a possible rise in productivity in the upper PETM body. This could have been prompted by an influx of nutrients to the basin, which could have been caused by an enhanced terrestrial sediment influx. An enhanced terrestrial sediment influx would bring substantial nutrients to the basin. However, but the low TAR values and the decrease in the CIA and kaolinite, as well as the dominance of marine organic matter (high HI>100; Fig. 10), rather suggest that sea-level rise and a decrease in the terrigenous influx dominate upwards in the PETM body. Alternatively However, the deposition of volcanic ash can work as a fertilizer, supplying key nutrients to the marine environment resulting in augmented productivity (Jones and Gislason, 2008). The post-PETM section at Fur is dominated by diatomite deposition, which could be a result of periodic rise in nutrient supply due to the voluminous ash deposition from the PETM recovery and onwards (Stokke et al., 2020a). Substantial increases in Ba and P₂O₅ occur after the deposition of Ash 39 at the end PETM body (Fig. 10; Table 4, Supplement 1). While there is limited evidence of ash deposition during the PETM body at Stolleklint, a Additional ash deposition below Ash - 39 have now been revealed by the possible cryptotephra in XRF element core scans (Fig. 6 section D). It could be that volcanic ash which could have had an added fertilizing effect promoting a rise in primary productivity during the later stages of the PETM body and recovery.~~

920 ~~The PETM carbon cycle perturbations are unusual both in magnitude and duration, and likely a result of a combination of triggers and feedback mechanisms that are not yet fully understood (McInerney and Wing, 2011; Komar and Zeebe, 2017).~~ A key PETM feature is the rapidity of the PETM recovery (e.g. Bowen and Zachos, 2010). Carbon cycle recovery occurs through a combination of natural carbon sequestration and negative feedback mechanisms reducing the atmospheric CO₂ content (McInerney and Wing, 2011). Silicate weathering and denudation is perhaps the most important negative feedback mechanisms driving CO₂ drawdown (Gislason and Oelkers, 2011), and have been proposed as one of the most important drivers during the PETM recovery (Kelly et al., 2005; Torfstein et al., 2010; Penman, 2016). However, Bowen and Zachos (2010) suggested that the rate of recovery is an order of magnitude faster than expected for carbon drawdown by silicate weathering alone. Similarly, Penman and Zachos (2018) found that the δ¹¹B and B/Ca records of ocean acidification recovers within
925
930

a similar time frame as the $\delta^{13}\text{C}$ record, and far more rapid than suggested by carbon cycle models that rely on silicate weathering alone (e.g. Zeebe et al., 2009). Similarly, Bowen and Zachos (2010) found that the rate of recovery is an order of magnitude faster than expected for carbon drawdown by silicate weathering alone, and suggested that terrestrial carbon sequestration may have played an important part. While our data can neither support nor contradict this theory, we We have documented a rise in nutrient supply and enhanced ~~primary export~~ productivity, which ~~would contribute~~ could lead to the increased organic carbon sequestration attributed to the accelerated PETM recovery (Bowen and Zachos, 2010; Komar and Zeebe, 2017; Bridgestock et al., 2019). Enhanced export productivity have also been observed in PETM sites globally (Bains et al., 2000; Egger et al., 2003; Stein et al., 2006; Soliman et al., 2011; Ma et al., 2014; Bridgestock et al., 2019), and average Ba burial rates approximately tripled during the PETM (Frieling et al., 2019). Our results show that negative feedback mechanisms responded rapidly to changes in carbon cycle and SSTs, and remained highly active from PETM onset to recovery. While the $\delta^{13}\text{C}$ values remained low until the PETM recovery, SSTs decreased gradually throughout the PETM body and recovery. This gradual decline may reflect a temperature response to the continued carbon drawdown by the alternating increases in both silicate weathering and export productivity during the PETM.

Conclusions

We present new mineralogical and geochemical data from Stolleklint, an expanded marine section at Fur in northwest Denmark covering the PETM onset, body and recovery. Here, the PETM is defined by a negative 4.5 % CIE and at least 10 °C temperature rise across the PETM onset. ~~The study focuses on a section at Stolleklint, where the PETM onset is seen as lithological shift from the Holmehus/Østerrende Formation bioturbated clays into the laminated clays of the Stolleklint Clay. The sediments are composed of marine clays, dominated by volcanogenic minerals such as smectite and zeolite, reflecting how the importance of the NAIP was as a source area during this period.~~

The CIE onset is ~~quickly~~ followed by an increase in kaolinite and the overall clay content, the chemical index of alteration, and substantially enhanced sedimentation rates. This reflects a rapid response in silicate weathering and transport patterns to changes in the carbon cycle and elevated temperatures, likely due to an enhanced hydrological cycle leading to erosion and sediment transport from the deeply weathered Fennoscandian shield. Large volumes of easily weathered NAIP flood basalts and widespread tephra deposits likely contributed to accelerate the degree of silicate weathering and carbon drawdown. This is reflected in the dominance of volcanogenic minerals such as smectite and zeolite in large parts of the stratigraphy.

Basin deoxygenation also begins to become widespread across the PETM onset, indicated by a shift from bioturbated to laminated sediments and extensive geochemical proxy evidence. Although the exact onset of deoxygenation is somewhat blurred pre-PETM due to ash deposition, our data show anoxic to sulfidic bottom-water conditions were prevalent from the CIE onset and became increasingly pervasive throughout the PETM body. Proxy evidence also indicate augmented export productivity towards the upper PETM body, coinciding with the reappearance of volcanic ash in XRF element core scans and in field exposures. Such a correlation highlights the fertilizing effect of volcanic nutrients, and its potential importance in increasing primary productivity. The continued deoxygenation throughout the PETM was likely caused by a combination of the basins already restricted nature, increased halocline stratification, and intensified export productivity.

975 ~~Proxy evidence shows augmented export productivity and organic matter burial towards the upper PETM body, coinciding with the reappearance of volcanic ash in XRF element core scans and in field exposures. Such a correlation highlights the fertilizing effect of volcanic nutrients, and its potential importance in increasing primary productivity. Pervasive basin deoxygenation also occurs shortly after the PETM onset, with anoxic to sulfidic euxinic bottom water conditions prevailing throughout the PETM body. The continued basin deoxygenation was likely caused by its already restricted nature combined with amplified terrestrial runoff leading to ocean stratification, and intensified export productivity.~~

980 The results presented in this study show the potentially rapid environmental response to changes in carbon cycle and temperature. Our data also show that negative feedback mechanisms were active throughout the PETM. ~~The increased export productivity in the upper PETM body and the renewed rise in kaolinite content and the CIA during the PETM recovery reflect the~~ and illustrates the important role of enhanced silicate weathering and organic matter burial in driving the carbon drawdown leading to the PETM recovery. This highlights the importance of such marginal marine areas in carbon sequestration and recovery from carbon cycle perturbations.

Data availability

985 All of the research data presented in this paper is publically available in the Supplement.

Author contributions

990 EWS, MTJ, and HHS conceptualized and laid out the methodology of the project. EWS, MTJ, LR, HH, IM, BPS, and HHS contributed to data collection and interpretations. MTJ, HH, and HHS contributed with funding acquisition. The original draft was prepared by EWS and MTJ. All authors contributed to the writing in the review and editing stage.

Competing interests

The authors declare that they have no conflict of interest

Acknowledgement

995 Claus Heilmann-Clausen, Sverre Planke, Christian Tegner, Tanusha Naidoo, Phil Holdship, Stephen Wyatt, Lina Hedvig Line, and Valentin Zuchuat are all warmly thanked for their assistance. This project was supported by the Research Council of Norway's funding schemes "Unge Forskerta" project number 263000 (project Ashlantic) and "Centres of Excellence" project number 223272.

References

1000 Abdelmalak, M. M., Planke, S., Faleide, J. I., Jerram, D. A., Zastrozhnov, D., Eide, S., & Myklebust, R. (2016). The development of volcanic sequences at rifted margins: New insights from the structure and morphology of the Vøring Escarpment, mid-Norwegian Margin. *Journal of Geophysical Research: Solid Earth*, 121(7), 5212-5236. <https://doi.org/10.1002/2015JB012788>

- 1005 Alegret, L., Ortiz, S., & Molina, E. (2009). Extinction and recovery of benthic foraminifera across the Paleocene–Eocene Thermal Maximum at the Alamedilla section (Southern Spain). *Palaeogeography, Palaeoclimatology, Palaeoecology*, 279(3-4), 186-200. <https://doi.org/10.1016/j.palaeo.2009.05.009>
- Algeo, T. J., & Tribovillard, N. (2009). Environmental analysis of paleoceanographic systems based on molybdenum–uranium covariation. *Chemical Geology*, 268(3-4), 211-225. <https://doi.org/10.1016/j.chemgeo.2009.09.001>
- 1010 Algeo, T. J., & Liu, J. (2020). A re-assessment of elemental proxies for paleoredox analysis. *Chemical Geology*, 540, 119549. <https://doi.org/10.1016/j.chemgeo.2020.119549>
- Alley, R. B. (2016). A heated mirror for future climate. *Science*, 352(6282), 151-152. DOI: 10.1126/science.aaf4837
- Anell, I., Thybo, H., & Rasmussen, E. (2012). A synthesis of Cenozoic sedimentation in the North Sea. *Basin Research*, 24(2), 154-179. <https://doi.org/10.1111/j.1365-2117.2011.00517.x>
- 1015 Babila, T. L., Penman, D. E., Hönisch, B., Kelly, D. C., Bralower, T. J., Rosenthal, Y., & Zachos, J. C. (2018). Capturing the global signature of surface ocean acidification during the Palaeocene–Eocene Thermal Maximum. *Philosophical Transactions of the Royal Society A: Mathematical, Physical and Engineering Sciences*, 376(2130), 20170072. <https://doi.org/10.1098/rsta.2017.0072>
- 1020 Bains, S., Norris, R. D., Corfield, R. M., & Faul, K. L. (2000). Termination of global warmth at the Palaeocene/Eocene boundary through productivity feedback. *Nature*, 407(6801), 171-174. <https://doi.org/10.1038/35025035>
- Behar, F., Beaumont, V., & Penteado, H. D. B. (2001). Rock-Eval 6 technology: performances and developments. *Oil & Gas Science and Technology*, 56(2), 111-134. <https://doi.org/10.2516/ogst:2001013>
- 1025 Bograd, S. J., Castro, C. G., Di Lorenzo, E., Palacios, D. M., Bailey, H., Gilly, W., & Chavez, F. P. (2008). Oxygen declines and the shoaling of the hypoxic boundary in the California Current. *Geophysical Research Letters*, 35(12), L12607. <https://doi.org/10.1029/2008GL034185>
- Bolle, M. P., Tantawy, A. A., Pardo, A., Adatte, T., Burns, S., & Kassab, A. (2000). Climatic and environmental changes documented in the upper Paleocene to lower Eocene of Egypt. *Eclogae Geologicae Helvetiae*, 93(1), 33-52. [10.5169/seals-168806](https://doi.org/10.5169/seals-168806)
- 1030 Bornemann, A., Norris, R. D., Lyman, J. A., D'haenens, S., Groeneveld, J., Röhl, U., ... & Speijer, R. P. (2014). Persistent environmental change after the Paleocene–Eocene Thermal Maximum in the eastern North Atlantic. *Earth and Planetary Science Letters*, 394, 70-81. <https://doi.org/10.1016/j.epsl.2014.03.017>
- Bowen, G. J. (2013). Up in smoke: A role for organic carbon feedbacks in Paleogene hyperthermals. *Global and Planetary Change*, 109, 18-29. <https://doi.org/10.1016/j.gloplacha.2013.07.001>
- 1035 Bowen, G. J., & Zachos, J. C. (2010). Rapid carbon sequestration at the termination of the Palaeocene–Eocene Thermal Maximum. *Nature Geoscience*, 3(12), 866-869. <https://doi.org/10.1038/ngeo1014>

- Bowen, G. J., Maibauer, B. J., Kraus, M. J., Röhl, U., Westerhold, T., Steimke, A., ... & Clyde, W. C. (2015). Two massive, rapid releases of carbon during the onset of the Palaeocene–Eocene thermal maximum. *Nature Geoscience*, 8(1), 44-47. <https://doi.org/10.1038/ngeo2316>
- 1040 Bridgestock, L., Hsieh, Y. T., Porcelli, D., & Henderson, G. M. (2019). Increased export production during recovery from the Paleocene–Eocene thermal maximum constrained by sedimentary Ba isotopes. *Earth and Planetary Science Letters*, 510, 53-63. <https://doi.org/10.1016/j.epsl.2018.12.036>
- Bøggild, O.B. (1918). Den vulkanske Aske i Moleret samt en Oversigt over Danmarks ældre Tertiærbjergarter. *Bulletin of the Geological Society of Denmark*, 33, 1-159.
- 1045 Carmichael, M. J., Inglis, G. N., Badger, M. P., Naafs, B. D. A., Behrooz, L., Remmelzwaal, S., ... & Dickson, A. J. (2017). Hydrological and associated biogeochemical consequences of rapid global warming during the Paleocene-Eocene Thermal Maximum. *Global and Planetary Change*, 157, 114-138. <https://doi.org/10.1016/j.gloplacha.2017.07.014>
- 1050 Carmichael, M. J., Pancost, R. D., & Lunt, D. J. (2018). Changes in the occurrence of extreme precipitation events at the Paleocene–Eocene thermal maximum. *Earth and Planetary Science Letters*, 501, 24-36. <https://doi.org/10.1016/j.epsl.2018.08.005>
- Cassidy, M., Watt, S. F., Palmer, M. R., Trofimovs, J., Symons, W., Maclachlan, S. E., & Stinton, A. J. (2014). Construction of volcanic records from marine sediment cores: A review and case study (Montserrat, West Indies). *Earth-Science Reviews*, 138, 137-155. <https://doi.org/10.1016/j.earscirev.2014.08.008>
- 1055 Charles, A. J., Condon, D. J., Harding, I. C., Pälike, H., Marshall, J. E., Cui, Y., ... & Croudace, I. W. (2011). Constraints on the numerical age of the Paleocene-Eocene boundary. *Geochemistry, Geophysics, Geosystems*, 12(6). <https://doi.org/10.1029/2010GC003426>
- 1060 Clausen, O. R., Nielsen, O. B., Huuse, M., & Michelsen, O. (2000). Geological indications for Palaeogene uplift in the eastern North Sea Basin. *Global and Planetary Change*, 24(3-4), 175-187. [https://doi.org/10.1016/S0921-8181\(00\)00007-2](https://doi.org/10.1016/S0921-8181(00)00007-2)
- Cramer, B. S., Toggweiler, J. R., Wright, J. D., Katz, M. E., & Miller, K. G. (2009). Ocean overturning since the Late Cretaceous: Inferences from a new benthic foraminiferal isotope compilation. *Paleoceanography*, 24(4). <https://doi.org/10.1029/2008PA001683>
- 1065 Cramwinckel, M. J., Huber, M., Kocken, I. J., Agnini, C., Bijl, P. K., Bohaty, S. M., ... & Peterse, F. (2018). Synchronous tropical and polar temperature evolution in the Eocene. *Nature*, 559(7714), 382-386. <https://doi.org/10.1038/s41586-018-0272-2>
- Croudace, I. W., Rindby, A., & Rothwell, R. G. (2006). ITRAX: description and evaluation of a new multi-function X-ray core scanner. In: Rothwell, R.G. (Ed.) *New Techniques in Sediment Core Analysis*. Geological Society, London, Special Publications, 267(1), 51-63. <https://doi.org/10.1144/GSL.SP.2006.267.01.04>

- 1070 Dickens, G. R., O'Neil, J. R., Rea, D. K., & Owen, R. M. (1995). Dissociation of oceanic methane hydrate as a cause of the carbon isotope excursion at the end of the Paleocene. *Paleoceanography and Paleoclimatology*, 10(6), 965-971. <https://doi.org/10.1029/95PA02087>
- Dickson, A. J., Rees-Owen, R. L., März, C., Coe, A. L., Cohen, A. S., Pancost, R. D., ... & Shcherbinina, E. (2014). The spread of marine anoxia on the northern Tethys margin during the Paleocene-Eocene Thermal Maximum. *Paleoceanography*, 29(6), 471-488. <https://doi.org/10.1002/2014PA002629>
- 1075 Dickson, A. J., Cohen, A. S., Coe, A. L., Davies, M., Shcherbinina, E. A., & Gavrillov, Y. O. (2015). Evidence for weathering and volcanism during the PETM from Arctic Ocean and Peri-Tethys osmium isotope records. *Palaeogeography, Palaeoclimatology, Palaeoecology*, 438, 300-307. <https://doi.org/10.1016/j.palaeo.2015.08.019>
- 1080 Doebelin, N., & Kleeberg, R. (2015). Profex: a graphical user interface for the Rietveld refinement program BGMN. *Journal of Applied Crystallography*, 48(5), 1573-1580. <https://doi.org/10.1107/S1600576715014685>
- Dunkley Jones, T., Lunt, D. J., Schmidt, D. N., Ridgwell, A., Sluijs, A., Valdes, P. J., & Maslin, M. (2013). Climate model and proxy data constraints on ocean warming across the Paleocene–Eocene Thermal Maximum. *Earth-Science Reviews*, 125, 123-145. <https://doi.org/10.1016/j.earscirev.2013.07.004>
- 1085 Dunkley Jones, T., Manners, H. R., Hoggett, M., Kirtland Turner, S., Westerhold, T., Leng, M. J., ... & Grimes, S. T. (2018). Dynamics of sediment flux to a bathyal continental margin section through the Paleocene–Eocene Thermal Maximum. *Climate of the Past*, 14(7), 1035-1049. <https://doi.org/10.5194/cp-14-1035-2018>
- Dypvik, H., Riber, L., Burca, F., Rütger, D., Jargvoll, D., Nagy, J., & Jochmann, M. (2011). The Paleocene–Eocene thermal maximum (PETM) in Svalbard—clay mineral and geochemical signals. *Palaeogeography, Palaeoclimatology, Palaeoecology*, 302(3-4), 156-169. <https://doi.org/10.1016/j.palaeo.2010.12.025>
- 1090 Egger, H., Heilmann-Clausen, C., & Schmitz, B. (2000). The Paleocene/Eocene-boundary interval of a Tethyan deep-sea section (Austria) and its correlation with the North Sea Basin. *Bulletin de la Société géologique de France*, 171(2), 207-216. <https://doi.org/10.2113/171.2.207>
- Egger, H., Fenner, J., Heilmann-Clausen, C., Rögl, F., Sachsenhofer, R.F., Schmitz, B. (2003). Paleoproductivity of the northwestern Tethyan margin (Anthering Sec-tion, Austria) across the Paleocene-Eocene transition. In: Wing, S.L., Gingerich, P.D., Schmitz, B., and Thomas, E. (Eds) *Causes and Consequences of Globally Warm Climates in the Early Paleogene*: Geological Society of America Special Paper 369, p. 133–146
- 1095 Eldholm, O., & Thomas, E. (1993). Environmental impact of volcanic margin formation. *Earth and Planetary Science Letters*, 117(3-4), 319-329. [https://doi.org/10.1016/0012-821X\(93\)90087-P](https://doi.org/10.1016/0012-821X(93)90087-P)
- 1100 Elrick, M., Polyak, V., Algeo, T. J., Romaniello, S., Asmerom, Y., Herrmann, A. D., ... & Chen, Z. Q. (2017). Global-ocean redox variation during the middle-late Permian through Early Triassic based on uranium isotope and Th/U trends of marine carbonates. *Geology*, 45(2), 163-166. <https://doi.org/10.1130/G38585.1>

- 1105 Frieling, J., Svensen, H. H., Planke, S., Cramwinckel, M. J., Selnes, H., & Sluijs, A. (2016). Thermogenic methane release as a cause for the long duration of the PETM. *Proceedings of the National Academy of Sciences*, 113(43), 12059-12064. <https://doi.org/10.1073/pnas.1603348113>
- Frieling, J., Gebhardt, H., Huber, M., Adekeye, O. A., Akande, S. O., Reichart, G. J., ... & Sluijs, A. (2017). Extreme warmth and heat-stressed plankton in the tropics during the Paleocene-Eocene Thermal Maximum. *Science Advances*, 3(3), e1600891. DOI: 10.1126/sciadv.1600891
- 1110 Frieling, J., Peterse, F., Lunt, D. J., Bohaty, S. M., Sinninghe-Damsté, J. S., Reichart, G. J., & Sluijs, A. (2019). Widespread warming before and elevated barium burial during the Paleocene-Eocene Thermal Maximum: Evidence for methane hydrate release?. *Paleoceanography and Paleoclimatology*, 34(4), 546-566. <https://doi.org/10.1029/2018PA003425>
- 1115 Gavrilov, Y. O., Kodina, L. A., Lubchenko, I. Y., & Muzylev, N. G. (1997). The late Paleocene anoxic event in epicontinental seas of Peri-Tethys and formation of the sapropelite unit: Sedimentology and geochemistry. *Lithology and Mineral Resources*, 32(5), 427-450. Translated from: *Litologiya i Poleznye Iskoparmye*, 5, 492-517.
- Gavrilov, Y. O., Shcherbinina, E. A., & Oberhansli, H. (2003). Paleocene-Eocene boundary events in the northeastern Peri-Tethys. In: Wing, S.L., Gingerich, P.D., Schmitz, B., and Thomas, El. (Eds.) *Special Papers, Geological Society of America*, 369, 147-168. <https://doi.org/10.1130/0-8137-2369-8.147>
- 1120 Gibbs, R. J. (1977). Clay mineral segregation in the marine environment. *Journal of Sedimentary Research*, 47(1), 237-243. <https://doi.org/10.1306/212F713A-2B24-11D7-8648000102C1865D>
- Gibson, T. G., Bybell, L. M., & Mason, D. B. (2000). Stratigraphic and climatic implications of clay mineral changes around the Paleocene/Eocene boundary of the northeastern US margin. *Sedimentary Geology*, 134(1-2), 65-92. [https://doi.org/10.1016/S0037-0738\(00\)00014-2](https://doi.org/10.1016/S0037-0738(00)00014-2)
- 1125 Gilly, W. F., Beman, J. M., Litvin, S. Y., & Robison, B. H. (2013). Oceanographic and biological effects of shoaling of the oxygen minimum zone. *Annual Review of Marine Science*, 5, 393-420. <https://doi.org/10.1146/annurev-marine-120710-100849>
- Gislason, S. R., & Oelkers, E. H. (2011). Silicate rock weathering and the global carbon cycle. In: Harmon, R.S. and Parker, A. (Eds.) *Frontiers in Geochemistry: Contribution of Geochemistry to the Study of the Earth*, 84-103. <https://doi.org/10.1002/9781444329957.ch5>
- 1130 Gutjahr, M., Ridgwell, A., Sexton, P. F., Anagnostou, E., Pearson, P. N., Pälike, H., ... & Foster, G. L. (2017). Very large release of mostly volcanic carbon during the Palaeocene–Eocene Thermal Maximum. *Nature*, 548(7669), 573-577. <https://doi.org/10.1038/nature23646>
- 1135 Haaland, H.J., Furnes, H., & Martinsen, O.J. (2000). Paleogene tuffaceous intervals, Grane Field (Block 25/11), Norwegian North Sea: their depositional, petrographical, geochemical character and regional implications. *Marine and Petroleum Geology*, 17(1), 101-118. [https://doi.org/10.1016/S0264-8172\(99\)00009-4](https://doi.org/10.1016/S0264-8172(99)00009-4)

- Harding, I. C., Charles, A. J., Marshall, J. E., Pälike, H., Roberts, A. P., Wilson, P. A., ... & Pearce, R. B. (2011). Sea-level and salinity fluctuations during the Paleocene–Eocene thermal maximum in Arctic Spitsbergen. *Earth and Planetary Science Letters*, 303(1-2), 97-107. <https://doi.org/10.1016/j.epsl.2010.12.043>
- 1140 Heilmann-Clausen C. (1994) Review of Paleocene dinoflagellates from the North Sea region. GFF 116, 51–53. Available at: <https://doi.org/10.1080/11035899409546149>.
- Heilmann-Clausen, C. (1995). Palæogene aflejringer over Danskekalken. In: Nielsen, O.B. (Ed.), *Aarhus Geokompender No. 1, Danmarks geologi fra Kridt til i dag*, pp. 69-114.
- Heilmann-Clausen, C., Nielsen, O. B., & Gersner, F. (1985). Lithostratigraphy and depositional environments in the Upper Paleocene and Eocene of Denmark. *Bulletin of the Geological Society of Denmark*, 33, 287-323.
- 1145 Held, I. M., & Soden, B. J. (2006). Robust responses of the hydrological cycle to global warming. *Journal of Climate*, 19(21), 5686-5699. <https://doi.org/10.1175/JCLI3990.1>
- Hembury, D. J., Palmer, M. R., Fones, G. R., Mills, R. A., Marsh, R., & Jones, M. T. (2012). Uptake of dissolved oxygen during marine diagenesis of fresh volcanic material. *Geochimica et Cosmochimica Acta*, 84, 353-368. <https://doi.org/10.1016/j.gca.2012.01.017>
- 1150 Hollis, C. J., Taylor, K. W., Handley, L., Pancost, R. D., Huber, M., Creech, J. B., ... & Gibbs, S. (2012). Early Paleogene temperature history of the Southwest Pacific Ocean: Reconciling proxies and models. *Earth and Planetary Science Letters*, 349-350, 53-66. <https://doi.org/10.1016/j.epsl.2012.06.024>
- Horni, J.A., Hopper, J.R., Blischke, A., Geisler, W.H., Stewart, M., McDermott, K., Judge, M., Elerlendsson, O., & Arting, U.E. (2017). Regional distribution of volcanism within the North Atlantic Igneous Province. In: Peron-Pinvidic, G., Hopper, J.R., Stoker, M.S., Gaina, C., Doornenbal, J.C., Funck, T., & Arting, U.E. (Eds.), *A Reappraisal of Crustal Structure, Tectonostratigraphy and Magmatic Evolution*. Geological Society, London, special publications. <https://doi.org/10.1144/SP447.18>
- 1155 Huggett, J. M., & Knox, R. O. B. (2006). Clay mineralogy of the Tertiary onshore and offshore strata of the British Isles. *Clay minerals*, 41(1), 5-46. <https://doi.org/10.1180/0009855064110195>
- 1160 Jenkyns, H. C. (2010). Geochemistry of oceanic anoxic events. *Geochemistry, Geophysics, Geosystems*, 11(3). <https://doi.org/10.1029/2009GC002788>
- John, C. M., Bohaty, S. M., Zachos, J. C., Sluijs, A., Gibbs, S., Brinkhuis, H., & Bralower, T. J. (2008). North American continental margin records of the Paleocene-Eocene thermal maximum: Implications for global carbon and hydrological cycling. *Paleoceanography*, 23(2). <https://doi.org/10.1029/2007PA001465>
- 1165 John, C. M., Banerjee, N. R., Longstaffe, F. J., Sica, C., Law, K. R., & Zachos, J. C. (2012). Clay assemblage and oxygen isotopic constraints on the weathering response to the Paleocene-Eocene thermal maximum, east coast of North America. *Geology*, 40(7), 591-594. <https://doi.org/10.1130/G32785.1>
- Jolley, D.W. & Widdowson, M. (2005). Did Paleogene North Atlantic rift-related eruptions drive early Eocene climate cooling? *Lithos*, 79, 355-366. <https://doi.org/10.1016/j.lithos.2004.09.007>

- 1170 Jones, M. T., & Gislason, S. R. (2008). Rapid releases of metal salts and nutrients following the deposition of volcanic ash into aqueous environments. *Geochimica et Cosmochimica Acta*, 72(15), 3661-3680. <https://doi.org/10.1016/j.gca.2008.05.030>
- Jones, M. T., Percival, L. M., Stokke, E. W., Frieling, J., Mather, T. A., Riber, L., ... & Svensen, H. H. (2019). Mercury anomalies across the Palaeocene–Eocene thermal maximum. *Climate of the Past*, 15(1).
1175 <https://doi.org/10.5194/cp-15-217-2019>
- Jordt, H., Thyberg, B. I., & Nøttvedt, A. (2000). Cenozoic evolution of the central and northern North Sea with focus on differential vertical movements of the basin floor and surrounding clastic source areas. *Geological Society, London, Special Publications*, 167(1), 219-243. <https://doi.org/10.1144/GSL.SP.2000.167.01.09>
- Kelly, D. C., Zachos, J. C., Bralower, T. J., & Schellenberg, S. A. (2005). Enhanced terrestrial weathering/runoff and surface ocean carbonate production during the recovery stages of the Paleocene-Eocene thermal maximum. *Paleoceanography*, 20(4). <https://doi.org/10.1029/2005PA001163>
- Kemp, S. J., Ellis, M. A., Mounteney, I., & Kender, S. (2016). Palaeoclimatic implications of high-resolution clay mineral assemblages preceding and across the onset of the Palaeocene–Eocene Thermal Maximum, North Sea Basin. *Clay Minerals*, 51(5), 793-813. <https://doi.org/10.1180/claymin.2016.051.5.08>
- 1185 Kender, S., Stephenson, M. H., Riding, J. B., Leng, M. J., Knox, R. W. B., Peck, V. L., ... & Jamieson, R. (2012). Marine and terrestrial environmental changes in NW Europe preceding carbon release at the Paleocene–Eocene transition. *Earth and Planetary Science Letters*, 353, 108-120. <https://doi.org/10.1016/j.epsl.2012.08.011>
- Kennett, J. P., & Stott, L. D. (1991). Abrupt deep-sea warming, palaeoceanographic changes and benthic extinctions at the end of the Palaeocene. *Nature*, 353(6341), 225-229. <https://doi.org/10.1038/353225a0>
- 1190 Kent, D. V., Cramer, B. S., Lanci, L., Wang, D., Wright, J. D., & Van der Voo, R. (2003). A case for a comet impact trigger for the Paleocene/Eocene thermal maximum and carbon isotope excursion. *Earth and Planetary Science Letters*, 211(1-2), 13-26. [https://doi.org/10.1016/S0012-821X\(03\)00188-2](https://doi.org/10.1016/S0012-821X(03)00188-2)
- Khozyem, H., Adatte, T., Spangenberg, J. E., Tantawy, A. A., & Keller, G. (2013). Palaeoenvironmental and climatic changes during the Palaeocene–Eocene Thermal Maximum (PETM) at the Wadi Nukhul Section, Sinai,
1195 Egypt. *Journal of the Geological Society*, 170(2), 341-352. <https://doi.org/10.1144/jgs2012-046>
- King C. (2016). *A Revised Correlation of Tertiary Rocks in the British Isles and Adjacent Areas of NW Europe* (Gale, A.S. & Barry, T.L., editors). Special reports, 27. The Geological Society, London.
- Kirtland Turner, S., Hull, P. M., Kump, L. R., & Ridgwell, A. (2017). A probabilistic assessment of the rapidity of PETM onset. *Nature communications*, 8(1), 1-10. <https://doi.org/10.1038/s41467-017-00292-2>
- 1200 Knox, R.O.B. & Morton, A.C. (1988). The record of early Tertiary N Atlantic volcanism in sediments of the North Sea Basin. In: Morton, A. C. & Parson, L. M. (Eds.) *Early Tertiary Volcanism and the Opening of the NE Atlantic*, *Geological Society, London, Special Publications*, 39(1), 407-419. <https://doi.org/10.1144/GSL.SP.1988.039.01.36>

- 1205 Knox, R. W. B. (1996). Tectonic controls on sequence development in the Palaeocene and earliest Eocene of southeast England: implications for North Sea stratigraphy. In: Hesselbo, S.P. & Parkinson, D.N. (Eds.) *Sequence Stratigraphy in British Geology*, Geological Society, London, Special Publications, 103(1), 209-230. <https://doi.org/10.1144/GSL.SP.1996.103.01.12>
- 1210 Knox, R.W.O'B., Bosch, J.H.A., Rasmussen, E.S., Heilmann-Clausen, C., Hiss, M., De Lugt, I.R., Kasinski, J., King, C., Köthe, A., Slodkowska, B., Standke, G., Vandenberghe, N. (2010). Cenozoic. In: Dornenbaal, H., Stevenson, A. (Eds.), *Petroleum Geological Atlas of the Southern Permian Basin Area*. EAGE Publications b.v, Houten, pp. 211–223.
- ~~Koch, P. L., Zachos, J. C., & Gingerich, P. D. (1992). Correlation between isotope records in marine and continental carbon reservoirs near the Palaeocene/Eocene boundary. *Nature*, 358(6384), 319-322. <https://doi.org/10.1038/358319a0>~~
- 1215 Komar, N., & Zeebe, R. E. (2017). Redox-controlled carbon and phosphorus burial: A mechanism for enhanced organic carbon sequestration during the PETM. *Earth and Planetary Science Letters*, 479, 71-82. <https://doi.org/10.1016/j.epsl.2017.09.011>
- 1220 Kraus, M. J., & Riggins, S. (2007). Transient drying during the Paleocene–Eocene Thermal Maximum (PETM): analysis of paleosols in the Bighorn Basin, Wyoming. *Palaeogeography, Palaeoclimatology, Palaeoecology*, 245(3-4), 444-461. <https://doi.org/10.1016/j.palaeo.2006.09.011>
- Lafargue, E., Marquis, F., & Pillot, D. (1998). Rock-Eval 6 applications in hydrocarbon exploration, production, and soil contamination studies. *Revue de l'institut français du pétrole*, 53(4), 421-437. <https://doi.org/10.2516/ogst:1998036>
- 1225 Larsen, L. M., Fitton, J. G., & Pedersen, A. K. (2003). Paleogene volcanic ash layers in the Danish Basin: compositions and source areas in the North Atlantic Igneous Province. *Lithos*, 71(1), 47-80. <https://doi.org/10.1016/j.lithos.2003.07.001>
- Larsen, R. B., & Tegner, C. (2006). Pressure conditions for the solidification of the Skaergaard intrusion: eruption of East Greenland flood basalts in less than 300,000 years. *Lithos*, 92(1-2), 181-197. <https://doi.org/10.1016/j.lithos.2006.03.032>
- 1230 Littler, K., Röhl, U., Westerhold, T., & Zachos, J.C. (2014). A high-resolution benthic stable-isotope record for the South Atlantic: Implications for orbital-scale changes in Late Paleocene–Early Eocene climate and carbon cycling. *Earth and Planetary Science Letters*, 401, 18-30. <https://doi.org/10.1016/j.epsl.2014.05.054>
- 1235 Ma, Z., Gray, E., Thomas, E., Murphy, B., Zachos, J., & Paytan, A. (2014). Carbon sequestration during the Palaeocene–Eocene Thermal Maximum by an efficient biological pump. *Nature Geoscience*, 7(5), 382-388. <https://doi.org/10.1038/ngeo2139>
- Marsh, R., Mills, R. A., Green, D. R., Salter, I., & Taylor, S. (2007). Controls on sediment geochemistry in the Crozet region. *Deep Sea Research Part II: Topical Studies in Oceanography*, 54(18-20), 2260-2274. <https://doi.org/10.1016/j.dsr2.2007.06.004>

- 1240 McInerney, F. A., & Wing, S. L. (2011). The Paleocene-Eocene Thermal Maximum: A perturbation of carbon cycle, climate, and biosphere with implications for the future. *Annual Review of Earth and Planetary Sciences*, 39, 489-516. <https://doi.org/10.1146/annurev-earth-040610-133431>
- McLennan, S. M. (1993). Weathering and global denudation. *The Journal of Geology*, 101(2), 295-303. <https://doi.org/10.1086/648222>
- 1245 McLennan, S. M. (2001). Relationships between the trace element composition of sedimentary rocks and upper continental crust. *Geochemistry, Geophysics, Geosystems*, 2(4). <https://doi.org/10.1029/2000GC000109>
- van der Meulen, B., Gingerich, P. D., Lourens, L. J., Meijer, N., van Broekhuizen, S., van Ginneken, S., & Abels, H. A. (2020). Carbon isotope and mammal recovery from extreme greenhouse warming at the Paleocene–Eocene boundary in astronomically-calibrated fluvial strata, Bighorn Basin, Wyoming, USA. *Earth and Planetary Science Letters*, 534, 116044. <https://doi.org/10.1016/j.epsl.2019.116044>
- 1250 Mitlehner, A. G. (1996). Palaeoenvironments in the North Sea Basin around the Paleocene-Eocene boundary: evidence from diatoms and other siliceous microfossils. *Geological Society, London, Special Publications*, 101(1), 255-273. <https://doi.org/10.1144/GSL.SP.1996.101.01.15>
- Moore, D.M., & Reynolds, R.C. (1997). *X-ray Diffraction and the Identification and Analysis of Clay Minerals*. Oxford University Press, Oxford.
- 1255 Morton, A. C., & Evans, J. A. (1988). Geochemistry of basaltic ash beds from the Fur Formation, Island of Fur, Denmark. *Bulletin of the Geological Society of Denmark*, 37(1-2), 1-9.
- Nagy, J., Jargvoll, D., Dypvik, H., Jochmann, M., & Riber, L. (2013). Environmental changes during the Paleocene–Eocene Thermal Maximum in Spitsbergen as reflected by benthic foraminifera. *Polar Research*, 32(1), 19737. <https://doi.org/10.3402/polar.v32i0.19737>
- 1260 Nesbitt, H., & Young, G. M. (1982). Early Proterozoic climates and plate motions inferred from major element chemistry of lutites. *Nature*, 299(5885), 715-717. <https://doi.org/10.1038/299715a0>
- Nielsen, O.B. & Heilmann-Clausen, C. (1988). Palaeogene volcanism: the sedimentary record in Denmark. *Geological Society, London, Special Publications*, 39(1), 395-405. <https://doi.org/10.1144/GSL.SP.1988.039.01.35>
- 1265 Nielsen, O. B., Sørensen, S., Thiede, J., & Skarbø, O. (1986). Cenozoic differential subsidence of North Sea. *AAPG bulletin*, 70(3), 276-298. <https://doi.org/10.1306/94885679-1704-11D7-8645000102C1865D>
- Nielsen, O. B., Rasmussen, E. S., & Thyberg, B. I. (2015). Distribution of clay minerals in the northern North Sea Basin during the Paleogene and Neogene: a result of source-area geology and sorting processes. *Journal of Sedimentary Research*, 85(6), 562-581. <https://doi.org/10.2110/jsr.2015.40>
- 1270 Nunes, F., & Norris, R. D. (2006). Abrupt reversal in ocean overturning during the Palaeocene/Eocene warm period. *Nature*, 439(7072), 60-63. <https://doi.org/10.1038/nature04386>

- Ogg, J., (2012). Geomagnetic Polarity Time Scale, in: Gradstein, F., Ogg, J., Schmitz, M., Ogg, G. (Eds.), *The Geologic Time Scale 2012*. Elsevier, pp. 85-113.
- 1275 Paytan, A., & Griffith, E. M. (2007). Marine barite: Recorder of variations in ocean export productivity. *Deep Sea Research Part II: Topical Studies in Oceanography*, 54(5-7), 687-705. <https://doi.org/10.1016/j.dsr2.2007.01.007>
- Pedersen, G. K., & Surlyk, F. (1983). The Fur Formation, a late Paleocene ash-bearing diatomite from northern Denmark. *Bulletin of the Geological Society of Denmark*, 32(1-2), 43-65.
- Pedersen, G. K., Pedersen, S. A. S., Steffensen, J., & Pedersen, C. S. (2004). Clay content of a clayey diatomite, the Early Eocene Fur Formation, Denmark. *Bulletin of the Geological Society of Denmark*, (51), 159-177.
- 1280 Pedersen, S. A. S. (2008). Palaeogene diatomite deposits in Denmark: geological investigations and applied aspects. *Geological Survey of Denmark and Greenland (GEUS) Bulletin*, 15, 21-24. <https://doi.org/10.34194/geusb.v15.5034>
- Penman, D. E. (2016). Silicate weathering and North Atlantic silica burial during the Paleocene-Eocene thermal maximum. *Geology*, 44(9), 731-734. <https://doi.org/10.1130/G37704.1>
- 1285 Penman, D. E., & Zachos, J. C. (2018). New constraints on massive carbon release and recovery processes during the Paleocene-Eocene Thermal Maximum. *Environmental Research Letters*, 13(10), 105008. <https://doi.org/10.1088/1748-9326/aae285>
- Petersen, H. I., Nielsen, L. H., Bojesen-Koefoed, J. A., Mathiesen, A., Kristensen, L., & Dalhoff, F. (2008). Evaluation of the quality, thermal maturity and distribution of potential source rocks in the Danish part of the Norwegian–Danish Basin. *Geological Survey of Denmark and Greenland Bulletin*, 16, 1-27. <https://doi.org/10.34194/geusb.v16.4989>
- 1290 Pujalte, V., Schmitz, B., & Baceta, J. I. (2014). Sea-level changes across the Paleocene–Eocene interval in the Spanish Pyrenees, and their possible relationship with North Atlantic magmatism. *Palaeogeography, Palaeoclimatology, Palaeoecology*, 393, 45-60. <https://doi.org/10.1016/j.palaeo.2013.10.016>
- 1295 Pälke, C., Delaney, M. L., & Zachos, J. C. (2014). Deep-sea redox across the Paleocene-Eocene thermal maximum. *Geochemistry, Geophysics, Geosystems*, 15(4), 1038-1053. <https://doi.org/10.1002/2013GC005074>
- Rasmussen, E. S., Heilmann-Clausen, C., Waagstein, R., & Eidvin, T. (2008). The tertiary of Norden. *Episodes*, 31(1), 66.
- 1300 Reynolds III, R. C., & Reynolds Jr, R. C. (2012). NEWMOD II a computer program for the calculation of one-dimensional diffraction patterns of mixed-layered clays. 1526 Farlow Avenue. *Crofton, MD, 21114*.
- Riahi, K., Van Vuuren, D. P., Kriegler, E., Edmonds, J., O’neill, B. C., Fujimori, S., ... & Lutz, W. (2017). The shared socioeconomic pathways and their energy, land use, and greenhouse gas emissions implications: an overview. *Global Environmental Change*, 42, 153-168. <https://doi.org/10.1016/j.gloenvcha.2016.05.009>

- 1305 Richter, T. O., Van der Gaast, S., Koster, B., Vaars, A., Gieles, R., de Stigter, H. C., ... & van Weering, T. C. (2006). The Avaatech XRF Core Scanner: technical description and applications to NE Atlantic sediments. *Geological Society, London, Special Publications*, 267(1), 39-50. <https://doi.org/10.1144/GSL.SP.2006.267.01.03>
- Rietveld, H. (1969). A profile refinement method for nuclear and magnetic structures. *Journal of applied Crystallography*, 2(2), 65-71. <https://doi.org/10.1107/S0021889869006558>
- 1310 Robert, C., & Kennett, J. P. (1994). Antarctic subtropical humid episode at the Paleocene-Eocene boundary: Clay-mineral evidence. *Geology*, 22(3), 211-214. [https://doi.org/10.1130/0091-7613\(1994\)022<0211:ASHEAT>2.3.CO:2](https://doi.org/10.1130/0091-7613(1994)022<0211:ASHEAT>2.3.CO:2)
- Rothwell, R. G. & Croudace, I. W. (2015). Twenty Years of XRF Core Scanning Marine Sediments: What Do Geochemical Proxies Tell Us? In: Croudace I., Rothwell R. (eds) *Micro-XRF Studies of Sediment Cores. Developments in Paleoenvironmental Research*, vol 17. Springer, Dordrecht, 25-102.
- 1315 Saunders, A.D. (2016). Two LIPs and two Earth-system crises: the impact of the North Atlantic Igneous Province and the Siberian Traps on the Earth-surface carbon cycle. *Geological Magazine*, 153, 201-222, <https://doi.org/10.1017/S0016756815000175>
- Schaller, M. F., Fung, M. K., Wright, J. D., Katz, M. E., & Kent, D. V. (2016). Impact ejecta at the Paleocene-Eocene boundary. *Science*, 354(6309), 225-229. DOI: 10.1126/science.aaf5466
- 1320 Schiøler, P., Andsbjerg, J., Clausen, O. R., Dam, G., Dybkjær, K., Hamberg, L., ... & Rasmussen, J. A. (2007). Lithostratigraphy of the Palaeogene–lower Neogene succession of the Danish North Sea. *GEUS Bulletin*, 12, 1-77. <https://doi.org/10.34194/geusb.v12.5249>
- | -Schmitz, B., & Pujalte, V. (2003). Sea-level, humidity, and land-erosion records across the initial Eocene thermal maximum from a continental-marine transect in northern Spain. *Geology*, 31(8), 689-692. <https://doi.org/10.1130/G19527.1>
- 1325 Schmitz, B., Peucker-Ehrenbrink, B., Heilmann-Clausen, C., Åberg, G., Asaro, F., & Lee, C. T. A. (2004). Basaltic explosive volcanism, but no comet impact, at the Paleocene–Eocene boundary: high-resolution chemical and isotopic records from Egypt, Spain and Denmark. *Earth and Planetary Science Letters*, 225(1-2), 1-17. <https://doi.org/10.1016/j.epsl.2004.06.017>
- 1330 Schoon, P. L., Heilmann-Clausen, C., Schultz, B. P., Sluijs, A., Sinninghe-Damsté, J. S., & Schouten, S. (2013). Recognition of Early Eocene global carbon isotope excursions using lipids of marine Thaumarchaeota. *Earth and Planetary Science Letters*, 373, 160-168. <https://doi.org/10.1016/j.epsl.2013.04.037>
- Schoon, P. L., Heilmann-Clausen, C., Schultz, B. P., Sinninghe-Damsté, J. S., & Schouten, S. (2015). Warming and environmental changes in the eastern North Sea Basin during the Palaeocene–Eocene Thermal Maximum as revealed by biomarker lipids. *Organic Geochemistry*, 78, 79-88. <https://doi.org/10.1016/j.orggeochem.2014.11.003>
- 1335

- Scott, C., & Lyons, T. W. (2012). Contrasting molybdenum cycling and isotopic properties in euxinic versus non-euxinic sediments and sedimentary rocks: Refining the paleoproxies. *Chemical Geology*, 324, 19-27. <https://doi.org/10.1016/j.chemgeo.2012.05.012>
- 1340 Seager, R., Naik, N., & Vecchi, G. A. (2010). Thermodynamic and dynamic mechanisms for large-scale changes in the hydrological cycle in response to global warming. *Journal of Climate*, 23(17), 4651-4668. <https://doi.org/10.1175/2010JCLI3655.1>
- Sluijs, A., Brinkhuis, H., Crouch, E. M., John, C. M., Handley, L., Munsterman, D., ... & Pancost, R. D. (2008). Eustatic variations during the Paleocene-Eocene greenhouse world. *Paleoceanography*, 23(4). <https://doi.org/10.1029/2008PA001615>
- 1345 <https://doi.org/10.1029/2008PA001615>
- Sluijs, A., Schouten, S., Donders, T. H., Schoon, P. L., Röhl, U., Reichart, G. J., ... & Brinkhuis, H. (2009). Warm and wet conditions in the Arctic region during Eocene Thermal Maximum 2. *Nature Geoscience*, 2(11), 777-780. <https://doi.org/10.1038/ngeo668>
- Sluijs, A., van Roij, L., Harrington, G. J., Schouten, S., Sessa, J. A., LeVay, L. J., Reichart, G.-J., & Slomp, C. P. (2014). Warming, euxinia and sea level rise during the Paleocene–Eocene Thermal Maximum on the Gulf Coastal Plain: implications for ocean oxygenation and nutrient cycling, *Climate of the Past*, 10, 1421–1439. <https://doi.org/10.5194/cp-10-1421-2014>
- 1350 <https://doi.org/10.5194/cp-10-1421-2014>
- Soliman, M. F., Aubry, M. P., Schmitz, B., & Sherrell, R. M. (2011). Enhanced coastal paleoproductivity and nutrient supply in Upper Egypt during the Paleocene/Eocene Thermal Maximum (PETM): Mineralogical and geochemical evidence. *Palaeogeography, Palaeoclimatology, Palaeoecology*, 310(3-4), 365-377. <https://doi.org/10.1016/j.palaeo.2011.07.027>
- 1355 <https://doi.org/10.1016/j.palaeo.2011.07.027>
- [Speijer, R.P., & Wagner, T. \(2002\). Sea-level changes and black shales associated with the late Paleocene thermal maximum: Organic-geochemical and micro-paleontologic evidence from the southern Tethyan margin \(Egypt-Israel\). In: Koeberl, C., & MacLeod, K.G. \(Eds.\) *Catastrophic Events and Mass Extinctions: Impacts and Beyond*. Geological Society of America Special Paper, 356, 533–549. DOI: 10.1130/0-8137-2356-6.533](#)
- 1360 [Speijer, R. P., Schmitz, B., & van der Zwaan, G. J. \(1997\). Benthic foraminiferal extinction and repopulation in response to latest Paleocene Tethyan anoxia. *Geology*, 25\(8\), 683-686.](#)
- Stefánsson, A., & Gíslason, S. R. (2001). Chemical weathering of basalts, Southwest Iceland: effect of rock crystallinity and secondary minerals on chemical fluxes to the ocean. *American Journal of Science*, 301(6), 513-556. <https://doi.org/10.2475/ajs.301.6.513>
- 1365 <https://doi.org/10.2475/ajs.301.6.513>
- Stein, R., Boucsein, B., & Meyer, H. (2006). Anoxia and high primary production in the Paleogene central Arctic Ocean: First detailed records from Lomonosov Ridge. *Geophysical Research Letters*, 33(18). <https://doi.org/10.1029/2006GL026776>
- <https://doi.org/10.1029/2006GL026776>
- Stokke, E. W., Jones, M. T., Tierney, J. E., Svensen, H. H., & Whiteside, J. H. (2020a). Temperature changes across the Paleocene-Eocene Thermal Maximum—a new high-resolution TEX86 temperature record from the Eastern North Sea Basin. *Earth and Planetary Science Letters*, 544, 116388. <https://doi.org/10.1016/j.epsl.2020.116388>
- 1370 <https://doi.org/10.1016/j.epsl.2020.116388>

- 1375 Stokke, E. W., Liu, E. J., & Jones, M. T. (2020b). Evidence of explosive hydromagmatic eruptions during the emplacement of the North Atlantic Igneous Province. *Volcanica*, 3(2), 227-250. <https://doi.org/10.30909/vol.03.02.227250>
- Storey, M., Duncan, R. A., & Swisher, C. C. (2007a). Paleocene-Eocene thermal maximum and the opening of the northeast Atlantic. *Science*, 316 (5824), 587-589. <https://doi.org/10.1126/science.1135274>
- 1380 Storey, M., Duncan, R.A., & Tegner, C. (2007b). Timing and duration of volcanism in the North Atlantic Igneous Province: Implications for geodynamics and links to the Iceland hotspot. *Chemical Geology*, 241(3), 264-281. <https://doi.org/10.1016/j.chemgeo.2007.01.016>
- Stramma, L., Johnson, G. C., Sprintall, J., & Mohrholz, V. (2008). Expanding oxygen-minimum zones in the tropical oceans. *Science*, 320(5876), 655-658. DOI: 10.1126/science.1153847
- 1385 Stramma, L., Prince, E. D., Schmidtko, S., Luo, J., Hoolihan, J. P., Visbeck, M., ... & Körtzinger, A. (2012). Expansion of oxygen minimum zones may reduce available habitat for tropical pelagic fishes. *Nature Climate Change*, 2(1), 33-37. <https://doi.org/10.1038/nclimate1304>
- Svensen, H., Planke, S., Malthes-Sørensen, A., Jamtveit, B., Myklebust, R., Eidem, T. R., & Rey, S. S. (2004). Release of methane from a volcanic basin as a mechanism for initial Eocene global warming. *Nature*, 429(6991), 542. <https://doi.org/10.1038/nature02566>
- 1390 Svensen, H. H., Bjærke, M. R., & Kverndokk, K. (2019). The Past as a Mirror: Deep Time Climate Change Exemplarity in the Anthropocene. *Culture Unbound*, 11(3-4), 330-352. <https://doi.org/10.3384/cu.2000.1525.1909301>
- Taylor, S. R., & McLennan, S. M. (1995). The geochemical evolution of the continental crust. *Reviews of Geophysics*, 33(2), 241-265. <https://doi.org/10.1029/95RG00262>
- 1395 Thiry, M. (2000). Palaeoclimatic interpretation of clay minerals in marine deposits: an outlook from the continental origin. *Earth-Science Reviews*, 49(1-4), 201-221. [https://doi.org/10.1016/S0012-8252\(99\)00054-9](https://doi.org/10.1016/S0012-8252(99)00054-9)
- Thomas, E., (1990). Late Cretaceous-early Eocene mass extinctions in the deep sea In: Sharpton, V. L. & Ward P. D. (Eds.) *Global catastrophes in Earth history; An interdisciplinary conference on impacts, volcanism, and mass mortality*. Geological Society of America Special Paper 247.
- 1400 Thomas, E., & Shackleton, N. J. (1996). The Paleocene-Eocene benthic foraminiferal extinction and stable isotope anomalies. *Geological Society, London, Special Publications*, 101(1), 401-441. <https://doi.org/10.1144/GSL.SP.1996.101.01.20>
- Torfstein, A., Winckler, G., & Tripathi, A. (2010). Productivity feedback did not terminate the Paleocene-Eocene Thermal Maximum (PETM). *Climate of the Past*, 6(2), 265-272. <https://doi.org/10.5194/cp-6-265-2010>
- 1405 Trenberth, K. E. (2011). Changes in precipitation with climate change. *Climate Research*, 47(1-2), 123-138. <https://doi.org/10.3354/cr00953>

- Tribovillard, N., Riboulleau, A., Lyons, T., & Baudin, F. (2004). Enhanced trapping of molybdenum by sulfurized marine organic matter of marine origin in Mesozoic limestones and shales. *Chemical Geology*, 213(4), 385-401. <https://doi.org/10.1016/j.chemgeo.2004.08.011>
- 1410 Tribovillard, N., Algeo, T. J., Lyons, T., & Riboulleau, A. (2006). Trace metals as paleoredox and paleoproductivity proxies: an update. *Chemical Geology*, 232(1-2), 12-32. <https://doi.org/10.1016/j.chemgeo.2006.02.012>
- Tribovillard, N., Algeo, T. J., Baudin, F., & Riboulleau, A. (2012). Analysis of marine environmental conditions based on molybdenum–uranium covariation—Applications to Mesozoic paleoceanography. *Chemical Geology*, 324, 46-58. <https://doi.org/10.1016/j.chemgeo.2011.09.009>
- 1415 Westerhold, T., Röhl, U., Wilkens, R. H., Gingerich, P. D., Clyde, W. C., Wing, S. L., Bowen, G. J., and Kraus, M. J. (2018). Synchronizing early Eocene deep-sea and continental records – cyclostratigraphic age models for the Bighorn Basin Coring Project drill cores, *Climate of the Past*, 14, 303-319. <https://doi.org/10.5194/cp-14-303-2018>
- 1420 Wieczorek, R., Fantle, M. S., Kump, L. R., & Ravizza, G. (2013). Geochemical evidence for volcanic activity prior to and enhanced terrestrial weathering during the Paleocene Eocene Thermal Maximum. *Geochimica et Cosmochimica Acta*, 119, 391-410. <https://doi.org/10.1016/j.gca.2013.06.005>
- Wignall, P. B., & Myers, K. J. (1988). Interpreting benthic oxygen levels in mudrocks: a new approach. *Geology*, 16(5), 452-455. [https://doi.org/10.1130/0091-7613\(1988\)016<0452:IBOLIM>2.3.CO;2](https://doi.org/10.1130/0091-7613(1988)016<0452:IBOLIM>2.3.CO;2)
- 1425 Wignall, P. B., & Twitchett, R. J. (1996). Oceanic anoxia and the end Permian mass extinction. *Science*, 272(5265), 1155-1158. DOI: 10.1126/science.272.5265.1155
- Wilkinson, C. M., Ganerød, M., Hendriks, B. W., & Eide, E. A. (2017). Compilation and appraisal of geochronological data from the North Atlantic Igneous Province (NAIP). *Geological Society, London, Special Publications*, 447(1), 69-103, <https://doi.org/10.1144/SP447.10>
- 1430 Yao, W., Paytan, A., & Wortmann, U. G. (2018). Large-scale ocean deoxygenation during the Paleocene-Eocene Thermal Maximum. *Science*, 361(6404), 804-806. DOI: 10.1126/science.aar8658
- Zachos, J. C., Röhl, U., Schellenberg, S. A., Sluijs, A., Hodell, D. A., Kelly, D. C., ... & McCarren, H. (2005). Rapid acidification of the ocean during the Paleocene-Eocene thermal maximum. *Science*, 308(5728), 1611-1615. DOI: 10.1126/science.1109004
- 1435 Zachos, J. C., Dickens, G. R., & Zeebe, R. E. (2008). An early Cenozoic perspective on greenhouse warming and carbon-cycle dynamics. *Nature*, 451(7176), 279-283. <https://doi.org/10.1038/nature06588>
- Zachos, J. C., McCarren, H., Murphy, B., Röhl, U., & Westerhold, T. (2010). Tempo and scale of late Paleocene and early Eocene carbon isotope cycles: Implications for the origin of hyperthermals. *Earth and Planetary Science Letters*, 299(1-2), 242-249. <https://doi.org/10.1016/j.epsl.2010.09.004>

- 1440 Zacke, A., Voigt, S., Joachimski, M. M., Gale, A. S., Ward, D. J., & Tütken, T. (2009). Surface-water freshening and high-latitude river discharge in the Eocene North Sea. *Journal of the Geological Society*, 166(5), 969-980. <https://doi.org/10.1144/0016-76492008-068>
- Zeebe, R. E., Zachos, J. C., & Dickens, G. R. (2009). Carbon dioxide forcing alone insufficient to explain Palaeocene–Eocene Thermal Maximum warming. *Nature Geoscience*, 2(8), 576-580. <https://doi.org/10.1038/ngeo578>
- 1445 Zhou, X., Thomas, E., Rickaby, R. E., Winguth, A. M., & Lu, Z. (2014). I/Ca evidence for upper ocean deoxygenation during the PETM. *Paleoceanography*, 29(10), 964-975. <https://doi.org/10.1002/2014PA002702>